AGU
ADVANCING EARTH AND SPACE SCIENCE

Representation of the Mean Atlantic Subtropical Cells in CMIP6 Models

Yao Fu[1] ID, Peter Brandt[2,3] ID, Franz Philip Tuchen[2,4] ID, Joke F. Lübbecke[2,3] ID, and Chunzai Wang[5] ID

[1]School of Earth and Atmospheric Sciences, Georgia Institute of Technology, Atlanta, GA, USA, [2]GEOMAR Helmholtz Centre for Ocean Research Kiel, Kiel, Germany, [3]Faculty of Mathematics and Natural Sciences, Kiel University, Kiel, Germany, [4]Now at NOAA/Atlantic Oceanographic and Meteorological Laboratory, Miami, FL, USA, [5]State Key Laboratory of Tropical Oceanography, South China Sea Institute of Oceanology, Chinese Academy of Sciences, Guangzhou, China

Abstract The Atlantic Subtropical Cells (STCs) consist of poleward Ekman transport in the surface layer, subduction in the subtropics, and equatorward transport in the thermocline layer that largely compensates the surface Ekman divergence and closes the STCs via equatorial upwelling. As a result, the STCs play an important role in connecting the tropical and subtropical Atlantic Ocean, in terms of heat, freshwater, oxygen, and nutrients exchange. However, their representation in state-of-the-art coupled models has not been systematically evaluated. In this study, we investigate the performance of the Coupled Model Intercomparison Project Phase 6 climate models in simulating the Atlantic STCs. Comparing model results with observations, we first present the simulated mean state with respect to ensembles of the key components participating in the STC loop, that is, the meridional Ekman and geostrophic flow across 10°N and 10°S, and the Equatorial Undercurrent (EUC) at 23°W. We find that the model ensemble reveals biases toward weak Southern Hemisphere Ekman transport and interior geostrophic transports, as well as a weak EUC. We then investigate the large inter-model spread of these key components and find that models with strong Ekman divergence between 10°N and 10°S tend to have strong mixed layer and thermocline interior convergence and strong EUC. The inter-model spread of the EUC strength is primarily associated with the intensity of the southeasterly trade winds in the models. Since the trade-wind-induced poleward Ekman transports are regarded as the drivers of the STCs, our results highlight the necessity to improve skills of coupled models to simulate the Southern Hemisphere atmospheric forcing.

Plain Language Summary This work systematically assesses how well state-of-the-art climate models simulate the Atlantic Subtropical Cells (STCs). The STCs are part of the shallow (upper 200 m) ocean circulation. They connect the upper tropical and subtropical Atlantic Ocean in each hemisphere via poleward transport in the surface layer (surface to about 100 m) and equatorward transport in the subsurface layer (100–200 m). Therefore, the STCs are important for the exchange of heat, freshwater, dissolved oxygen, and nutrients between these regions. In this work, we find that the climate models generally simulate a too weak Southern Hemisphere STC which can be related to weaker southeasterly trade winds compared to observations. The results highlight the necessity to improve the ability of coupled climate models to realistically simulate the winds in the Southern Hemisphere, in order to better simulate the tropical-subtropical ocean circulation. The results provide an important reference for studies on the mean state and variability of the Atlantic STCs, and for studies investigating the STCs' possible change in the future under global warming using coupled climate models.

1. Introduction

The upper layers of the tropical and subtropical oceans are connected by shallow meridional overturning circulations termed the Subtropical Cells (STCs). In a zonally-averaged, two-dimensional view, the STCs consist of a poleward mixed-layer branch that carries the upwelled water from the equator to the subtropics (up to about 30°N/S), and an equatorward and predominantly westward thermocline branch that transports subducted waters from the subtropics to the equatorial region. Subsequently, the converged thermocline water largely joins the Equatorial Undercurrent (EUC) and is transported to the eastern equatorial and eastern boundary upwelling regions to complete the STC loop (Graffino et al., 2021; Schott et al., 2004; Zhang et al., 2003). As a result, the STCs in both the Atlantic and Pacific are found to modulate equatorial sea surface temperature (SST) on interannual to decadal timescales via equatorward volume transport changes (Graffino et al., 2021; Kleeman et al., 1999;

McCreary & Lu, 1994; McPhaden & Zhang, 2002; Tuchen et al., 2020). In addition, changes in STC transports could potentially affect thermocline oxygen ventilation by changing the equatorward supply of newly subducted oxygen-rich water (Brandt et al., 2015, 2021; Duteil et al., 2014; Oschlies et al., 2018) or nutrient transport toward the upwelling regions impacting biological productivity (Duteil et al., 2014). Therefore, the STCs play an important role in the tropical-subtropical climate and ecological systems due to their role in the meridional and zonal heat, freshwater, oxygen, and nutrients distribution.

Observational and model studies have revealed the existence of different pathways of the STC branches (Johnson & Zhang, 2003; Liu et al., 1994; Malanotte-Rizzoli et al., 2000; Rabe et al., 2008; Tuchen et al., 2019), leading to a much more complex picture of the STCs compared to the simplified two-dimensional view. In the subtropical Atlantic, subduction mainly occurs in the eastern basin due to Ekman pumping. The subducted water is advected westward and equatorward, following the western boundary and interior pathways (Karstensen & Quadfasel, 2002). However, in the Northern Hemisphere, the positive wind stress curl under the seasonally migrating Intertropical Convergence Zone forms a barrier of high potential vorticity in the eastern part of the basin, which forces the interior thermocline water to take a westward detour in order to move further equatorward (Malanotte-Rizzoli et al., 2000; Schott et al., 2004; Zhang et al., 2003).

The STC pathways in the tropical Atlantic are further complicated by the warm upper limb of the Atlantic Meridional Overturning Circulation (AMOC) that flows northward throughout the entire Atlantic Ocean. In particular, a large portion of the AMOC's upper limb passes along the western boundary (e.g., Tuchen et al., 2022). The western boundary current (WBC) in the upper tropical South Atlantic is the North Brazil Undercurrent (NBUC), which is well-established north of 12°S with a subsurface core below the main thermocline (e.g., Hummels et al., 2015; Schott et al., 2005). When the NBUC flows northward, it is joined by the central branch of the South Equatorial Current (cSEC) north of about 5°S. The continuation of both currents, NBUC und cSEC, forms the surface-intensified North Brazil Current (NBC) that crosses the equator and undergoes a seasonally-varying retroflection north of the equator (Schott et al., 2004). The upper ocean WBC consists of contributions from the AMOC, the STCs and the Sverdrup circulation. The latter is composed of the clockwise equatorial gyre between 15°S and 5°N and the anti-clockwise tropical gyre to the north (Fratantoni et al., 2000). The superposition of the AMOC, STCs and Sverdrup circulation causes an asymmetric structure of the STCs between the Northern and Southern Hemisphere, that is, a stronger equatorward thermocline transport in the South Atlantic relative to a weaker thermocline STC component in the North Atlantic (Tuchen et al., 2022). Due to the asymmetric contribution to equatorward thermocline convergence between the North and South Atlantic, the EUC is overwhelmingly supplied by water originating from the South Atlantic (Fratantoni et al., 2000; Hazeleger et al., 2003). In a numerical experiment by Fratantoni et al. (2000), approximately 85% of the EUC transport at 40°W originates from the South Atlantic.

Observation-based estimates of the Atlantic STCs are rare. Zhang et al. (2003) used historical hydrographic data to estimate the mean strength of the Atlantic STCs. They determined a mean poleward surface layer divergence of 21 Sv between 6°S and 10°N, which is supplied by a mean equatorward thermocline convergence of 15 Sv (10 Sv from the South Atlantic and 5 Sv from the North Atlantic) and 6 Sv upwelled from beneath the thermocline associated with the upper limb of the AMOC. Based on Argo data, Tuchen et al. (2019) estimated the mean Atlantic STCs with a net poleward divergence of 14.6 ± 3.4 Sv in the surface layer and a net equatorward convergence of 11.9 ± 1.7 Sv in the thermocline. A net imbalance of 2.7 ± 3.8 Sv is attributed to upwelling from beneath the thermocline related to the AMOC upper limb. The contribution of the South and North Atlantic to the thermocline convergence is 9 and 2.9 Sv, respectively. Though the estimates of Zhang et al. (2003) and Tuchen et al. (2019) differ in the mean STC strength, both studies confirm that the equatorward thermocline transport of the southern STC branch is more than double that of the northern STC branch. Based on an updated Argo data set, Tuchen et al. (2020) further inferred the variability of the Atlantic STCs and found that the interior thermocline convergence modulates sea surface temperature (SST) in the equatorial and eastern tropical upwelling region on timescales of 5 years and longer, which is in agreement with previous results from a data assimilation model (Rabe et al., 2008). This highlights the importance of the STCs in the tropical and subtropical climate system.

By using a high-resolution global ocean model with 0.25° horizontal resolution and 36 vertical levels, Hazeleger and Drijfhout (2006) estimated the mean strength of the Atlantic STCs with the southern branch accounting for only 4 Sv and the northern branch for 1.5 Sv. This is more than two times smaller than the estimates based on observed hydrography (Tuchen et al., 2019; Zhang et al., 2003). Based on output from the assimilation model

GECCO, Rabe et al. (2008) found a mean equatorward flow in the thermocline of 16.5 Sv at 10°S and 3.8 Sv at 10°N. The analysis of GECCO output also indicates that on timescales longer than 5 years enhanced surface Ekman divergence drives the equatorial upwelling, which leads to a strengthened EUC, followed by convergence in the thermocline. This suggests a pulling mechanism by the wind and highlights the role of the EUC in closing the STC loop.

Despite the observational and ocean-modeling studies mentioned above, the representation of the Atlantic STCs in state-of-the-art coupled climate models has not yet been systematically investigated. In this study, we use output from models of the Coupled Model Intercomparison Project Phase 6 (CMIP6) to evaluate the ability of the coupled models to reproduce the mean state of the Atlantic STCs and to determine the links between the different mean STC components among the models. The results provide a reference for studies on the mean state and variability of the STCs, as well as for assessment of the STCs' possible change under global warming using coupled climate models.

The CMIP6 models and other data, such as wind stress and Argo climatology used in this study are described in Section 2. In Section 3, the mean state of the STC loop components, including the Ekman and geostrophic transports across 10°N and 10°S, and the EUC at 23°W are presented. The inter-model relationship among the mean STC loop components and between the STC and the AMOC are investigated in Section 4. The results are finally summarized and discussed in Section 5.

2. Data and Methods

In this study, we focus on the mean state of the Atlantic STCs by analyzing output from the "historical" simulations of 28 CMIP6 coupled models (Table 1). The historical simulations are forced by evolving observed natural and anthropogenic changes in atmospheric compositions and cover most of the industrial period from 1850 to present (Eyring et al., 2016). These simulations allow to evaluate the coupled climate models' ability to simulate the mean state, variability, and trend of the present-day climate, which will improve our understanding of both current and future climate change. In order to facilitate calculations and comparisons among the models, the outputs of all models on their native grids are first linearly interpolated onto a uniform $0.5° \times 0.5°$ horizontal grid. Note that as most of the CMIP6 models have a 1° zonal resolution, the horizontal interpolation should well resolve the original model field and have a marginal impact on the calculation results.

We calculate meridional transports across 10°N and 10°S to represent the Atlantic STC in the Northern and Southern Hemisphere (Figure 1). The two latitudes have been previously used in STC studies based on observations (Tuchen et al., 2019, 2020) and models (Rabe et al., 2008), which facilitates our comparison with previous studies. Futhermore, the two latitudes are distant enough from the equator, thus not being impacted by the Tropical Cells that are narrowly confined around the equator (Schott et al., 2004). The Ekman divergence caused by the trade winds is regarded as the forcing of the STCs. Therefore, we first calculate the meridional Ekman transports at 10°N and 10°S using the wind stress data from each model as follows:

$$M_{Ek}^{y} = -\frac{1}{\rho_0} \frac{\tau_x}{f} \qquad (1)$$

where τ_x is the zonal wind stress, ρ_0 is the density of sea water with a constant value of 1,025 kg m^{-3}, and f is the Coriolis parameter. The Ekman divergence between the two latitudes is the sum of the northward and southward Ekman transports at 10°N and 10°S, respectively. Note that CMIP6 models provide surface wind stress both from the atmospheric component (with variable name "tauu") and from the oceanic component ("tauuo"). Throughout this study, we used "tauuo" when it is available. For the models "BCC-CSM2-MR", "BCC-ESM1" and "MIROC6", "tauuo" is not provided. We instead used "tauu" and removed data points on land for the calculation.

To quantify the Atlantic STC transports, we calculate the total and geostrophic transports at 10°N and 10°S. We first divide the STC transports vertically into two components, namely the mixed layer (ML) transport and the thermocline transport. The mixed layer depth (MLD) is defined as the depth, at which the potential density is 0.125 kg m^{-3} larger than the value at the shallowest depth of a model. The lower boundary of the thermocline transport is defined by the 26.4 kg m^{-3} isopycnal (surface of constant potential density, σ_θ). Note that this isopycnal is larger than the 26.0 kg m^{-3} selected by Tuchen et al. (2019). This is because in this study we also investigate the EUC as a component of the STC loop, and the 26.4 kg m^{-3} isopycnal covers the bottom of the EUC core (see

Table 1
Information of the Coupled Model Intercomparison Project Phase 6 Historical Simulations Used in This Study

Model name	Nation/Region	Ocean model name, horizontal resolution, and number of vertical levels
ACCESS-CM2	Australia	MOM5, 1° × 1°, 50 levels
ACCESS-ESM1-5	Australia	MOM5, 1° × 1°, 50 levels
BCC-CSM2-MR	China	MOM4, 1/3° × 1°, 40 levels
BCC-ESM1	China	MOM4, 1/3° × 1°, 40 levels
CAMS-CSM1-0	China	MOM4, 1/3° × 1°, 50 levels
CAS-ESM2-0	China	LICOM2.0, 1° × 1°, 30 levels
CESM2	USA	POP2, 1/3° × 1°, 60 levels
CESM2-WACCM	USA	POP2, 1/3° × 1°, 60 levels
CESM2-FV2	USA	POP2, 1/3° × 1°, 60 levels
CESM2-WACCM-FV2	USA	POP2, 1/3° × 1°, 60 levels
CanESM5	Canada	NEMO3.4.1, 1/3° × 1°, 45 levels
E3SM-1-0	USA	MPAS-Ocean, 1° × 1°, 60 levels
E3SM-1-1	USA	MPAS-Ocean, 1° × 1°, 60 levels
E3SM-1-1-ECA	USA	MPAS-Ocean, 1° × 1°, 60 levels
EC-Earth3	Europe	NEMO3.6, 1/3° × 1°, 75 levels
EC-Earth3-Veg	Europe	NEMO3.6, 1/3° × 1°, 75 levels
FIO-ESM-2-0	China	POP2-W, 1/3° × 1°, 60 levels
GFDL-CM4	USA	GFDL-OM4p25, 0.25° × 0.25°, 75 levels
HadGEM3-GC31-LL	UK	NEMO-HadGEM3-GO6.0 1° × 1°, 75 levels
HadGEM3-GC31-MM	UK	NEMO-HadGEM3-GO6.0 0.25° × 0.25°, 75 levels
IPSL-CM6A-LR	France	NEMO-OPA, 1° × 1°, 75 levels
MCM-UA-1-0	USA	MOM1.0, 1.875° × 2.5°, 18 levels
MIROC6	Japan	COCO4.9, 1° × 1°, 63 levels
MPI-ESM-1-2-HAM	Germany	MPIOM1.63, approx. 1.5° × 1.5°, 40 levels
MPI-ESM1-2-HR	Germany	MPIOM1.63, approx. 0.4° × 0.4°, 40 levels
MPI-ESM1-2-LR	Germany	MPIOM1.63, approx. 1.5° × 1.5°, 40 levels
MRI-ESM2-0	Japan	MRI.COM4.4, 0.5° × 1°, 61 levels
SAM0-UNICON	South Korea	POP2, 1/3°×1°, 60 levels

Section 3.4). Transport from the surface to the MLD is referred to as ML transport, and transport between the MLD and 26.4 kg m^{-3} is referred to as thermocline layer transport.

We then horizontally divide each layer into a western boundary component, an interior component, and an eastern boundary component. The western boundary is defined as the region west of 55°W (32°W) at 10°N (10°S), while the eastern boundary is defined as the region east of 25°W (0°E) at 10°N (10°S). The interior is the region between the western and eastern boundary. The total transport components are calculated by integrating the meridional velocity of a model simulation within the respective regions and layers. The geostrophic transport components are calculated by integrating the meridional geostrophic velocity. The geostrophic velocity shear is derived based on the thermal wind relation using the model density field referenced to 200 m. The model meridional velocity at 200 m is used as the reference velocity to obtain the absolute meridional geostrophic velocity (see Section 3.3 for comparison between ensemble meridional total velocity and geostrophic velocity). The reference depth of 200 m is well below the MLD or the top of the pycnocline with flow in geostrophic balance in the tropical Atlantic Ocean (Fu et al., 2017). At the position where the water depth in a model is shallower than 200 m, the bottom depth and bottom velocity are used as reference.
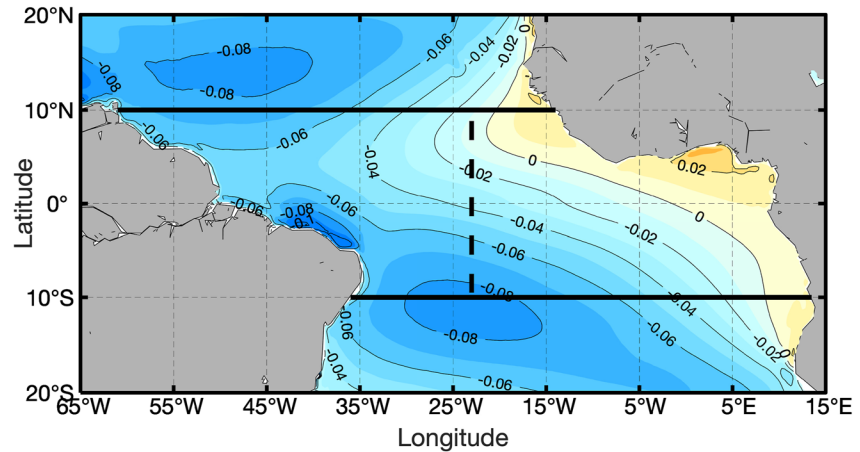
Figure 1. Mean zonal wind stress (N m^{-2}) in the tropical Atlantic from the National Centers for Environmental Prediction/Climate Forecast System Reanalysis data set for the time period from 1979 to 2010. The 10°N and 10°S sections are marked with the solid zonal black thick lines. The 23°W section is marked with the dashed meridional black thick line.

In order to investigate the relationship between the EUC and other STC components in the Atlantic, we select a meridional section along 23°W to characterize the EUC (Figure 1). Long-term hydrographic and current observations are available along the 23°W section (Brandt et al., 2021), which can be used to validate the modeled EUC. The EUC transport for all models is calculated by integrating the eastward velocity in the upper 200 m between 2°N and 2°S at 23°W.

The focus of this study is the mean state of the Atlantic STCs. Therefore, for each model, a climatological mean of each variable described above is calculated by averaging over the full model period. Model ensembles of the variables are obtained by averaging the climatological means of all models.

Results of the CMIP6 model analysis are compared with observations. For hydrographic properties, we use an Argo mean field (Roemmich & Gilson, 2009, hereafter Argo climatology) with 1/6° horizontal resolution and 58 vertical levels in the upper 2,000 m. The data set includes data for the period from 2004 to 2018. Mean geostrophic velocity sections at 10°N and 10°S in the Atlantic are estimated based on the Argo mean. Here, a level of no motion at 1,200 m is applied and a topographic mask is used to exclude data points below the sea bottom which occur due to the extrapolation methods of the data product. In addition, we use two wind stress datasets to validate the model wind field and model-based Ekman transports, namely the monthly National Centers for Environmental Prediction Climate Forecast System Reanalysis (NCEP/CFSR, Decker et al., 2012) wind stress data with 1° × 1° horizontal resolution covering the period from 1979 to 2010, and ASCAT wind stress data with 0.25° × 0.25° covering the period from 2007 to 2019 provided by the Copernicus Marine Environmental Monitoring Service (CMEMS). Furthermore, a mean zonal velocity section at 23°W calculated from 31 repeated shipboard ADCP sections is used to validate the modeled mean EUC. The ADCP data used here is the same as published in Brandt et al. (2021).

3. Mean State of the Atlantic STC and EUC

The ensemble meridional overturning streamfunction in the upper 300 m between 30°N and 30°S shows the shallow overturning cells (i.e., the STCs) in both hemispheres (Figure 2). The overturning streamfunction is calculated by integrating the meridional velocity zonally and cumulatively from the surface downwards. In the Southern Hemisphere, the negative streamfunction with a minimum at about 13°S represents the southern STC with an anticlockwise circulation. Southward Ekman transport in the Southern Hemisphere dominates in the upper 50 m, which is balanced by the equatorward geostrophic flow in the upper 110–140 m as indicated by the 0-streamline. Note that this depth is clearly shallower than the ensemble mean depth (172.5 m) of the 26.4 kg m^{-3} isopycnal that is used to represent the bottom of the STCs. This is due to the superposition of the AMOC, which reduces the southward ML transport and enhances the northward thermocline transport in the Southern Hemisphere and results in a shallower closed cell in the streamfunction. Near the equator, about 5 Sv transport from the South
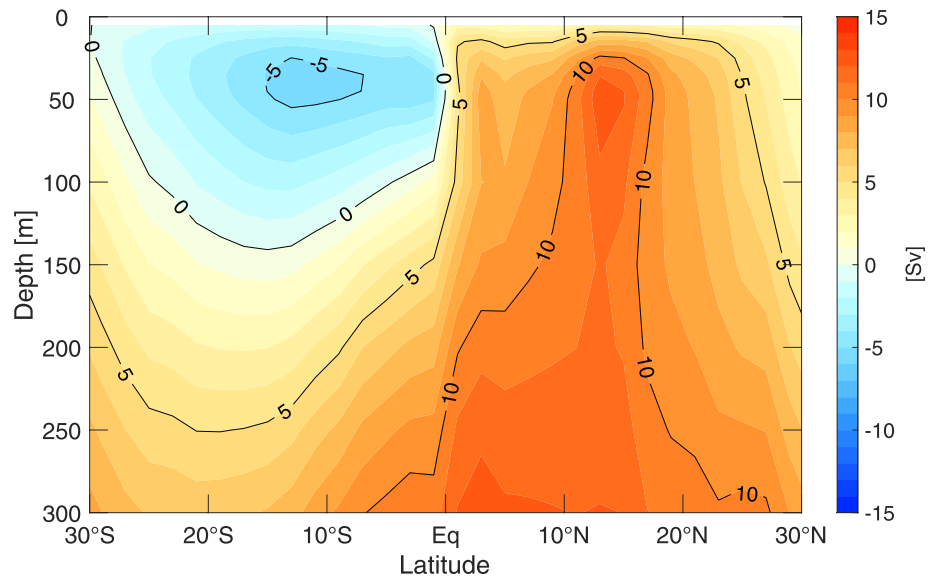
Figure 2. Ensemble mean Subtropical Cells streamfunction of the 28 Coupled Model Intercomparison Project Phase 6 models. The streamfunction is calculated by integrating the meridional velocity zonally and cumulatively from the surface downwards. Blue shading indicates an anticlockwise circulation, while red shading indicates a clockwise circulation. The contour lines are drawn with a transport interval of 5 Sv.

Atlantic is upwelled to the surface and continues northward in the surface layer. In the Northern Hemisphere, the STC is centered at about 14°N, where the maximum northward Ekman transport induced by the trade winds is located (Fu et al., 2017). The equatorward thermocline transport does not fully compensate for the poleward transport in the surface layer, due to the coexistence of the upper limb of the AMOC (Wang & Zhang, 2013). However, the thermocline STC component is still evident through the slight decrease of the streamfunction from its peak at about 50 m to a minimum at about 150 m.

In the following, to investigate the mean state of the STCs simulated by the CMIP6 models, we examine model ensembles of the key components participating in the STC loop at selected locations, that is, the meridional Ekman transport and geostrophic flow at 10°N and 10°S, and the Equatorial Undercurrent at 23°W, and compare these components with the observations.

3.1. Ekman Transport

We proceed with the forcing components of the STCs, that is, the poleward Ekman transports at 10°N and 10°S (Figure 3). From west to east, the cumulative meridional Ekman transports increase almost linearly in the westernmost two thirds of the basin west of 25°W (0°E) at 10°N (10°S). In the eastern third of the basin, the cumulative Ekman transports change only slightly, indicating very weak Ekman transport in this segment. The Ekman transports differ greatly among the models, leading to a large inter-model spread of the total Ekman transports in both hemispheres (5.5 to 12.4 Sv at 10°N and −5.0 to −11.8 Sv at 10°S, "−" indicates southward). The ensemble Ekman transport at 10°N (9.6 ± 1.6 Sv, mean ± standard deviation of the 28 models) aligns well with the NCEP/CFSR and ASCAT Ekman transport (9.6 ± 0.5 Sv for NCEP/CFSR and 10.6 ± 0.9 Sv for ASCAT, mean ± standard error of the mean) throughout the section (Figure 3a), while the ensemble Ekman transport at 10°S (−9.3 ± 1.7 Sv) is consistently weaker than the NCEP/CFSR (−11.2 ± 2.0 Sv) and ASCAT (12.0 ± 0.4 Sv) Ekman transports (Figure 3b). The generally weak modeled meridional Ekman transport in the Southern Hemisphere is also evident from the individual models. As the meridional Ekman transport is derived directly from the zonal wind stress (Equation 1), the generally weak Ekman transport at 10°S suggests a weak modeled wind field in the Southern Hemisphere. Zonal wind stress pattern derived from the NCEP/CFSR mean and model ensemble (Figure S1 in Supporting Information S1) shows that the ensemble maximum zonal wind stress over the South Atlantic is located further south compared to the observations. This results in a weaker simulated zonal wind stress at 10°S. The zonal wind stress bias in the Northern Hemisphere is less pronounced compared to that in the
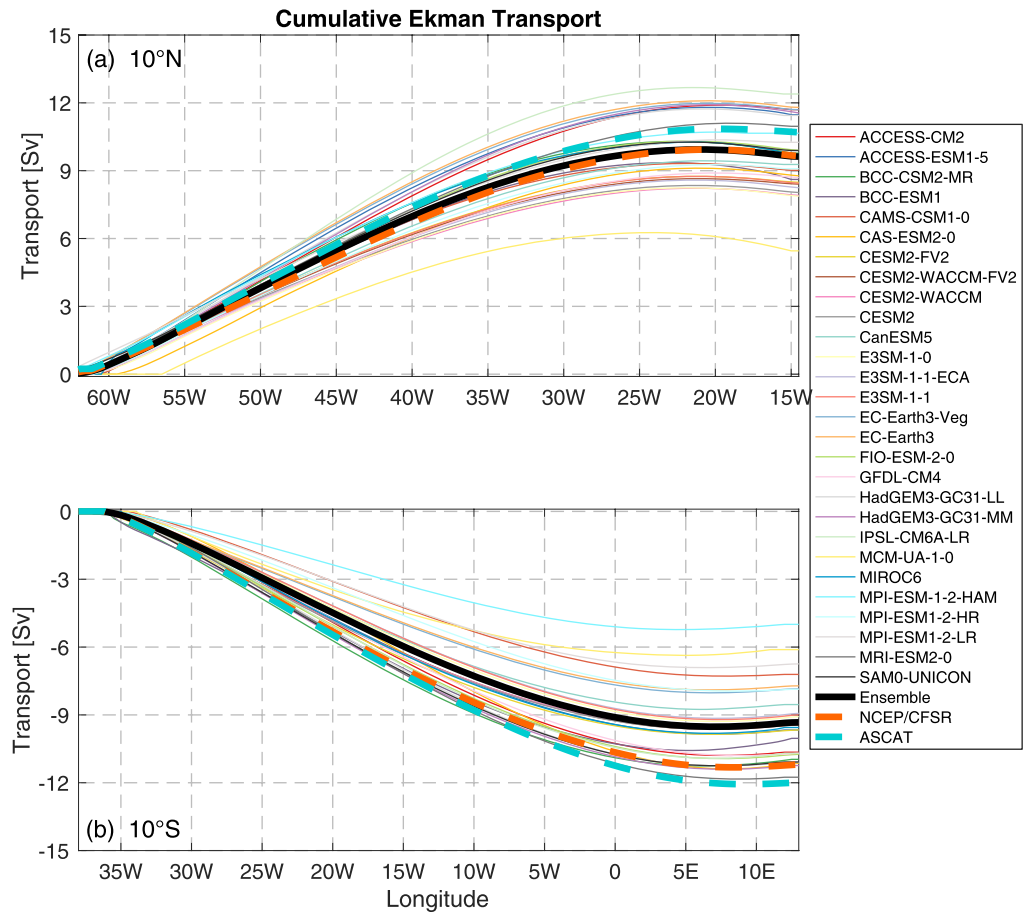
Figure 3. Cumulative meridional Ekman transport integrated from west to east (a) at 10°N and (b) at 10°S. The thin colored lines are estimated from individual models. The black thick line is the multi-model ensemble. The orange dashed thick line is calculated from National Centers for Environmental Prediction/Climate Forecast System Reanalysis. The cyan dashed thick line is calculated from ASCAT.

Southern Hemisphere in terms of a meridional shift of the maximum zonal wind stress. Therefore, the ensemble Ekman transport at 10°N is consistent with the NCEP/CFSR Ekman transport.

3.2. Hydrography at 10°N and 10°S

It is important to examine the hydrography at 10°N and 10°S in the models, since the basin-scale zonal density structure set by the hydrography has large impact on the meridional geostrophic flow, which counteracts the poleward Ekman transports. Compared to the Argo climatology (averaged between January 2004 and December 2018), the model ensemble at 10°N appears to be cooler in the mixed layer but warmer in the thermocline layer and beneath (Figures 4a, 4c and 4e). Overall, the magnitude of the cold and warm biases is relatively small (mostly less than 1°C), except for a warm bias core ($\Delta\theta > 2$°C) between 100 and 200 m and between 50°W and 45°W. As a result, the ensemble warm bias weakens the local density gradient between 55°W and 50°W (Figure 4g). Later we will show that such a local density bias causes non-negligible differences in the interior thermocline transport between the CMIP6 ensemble and Argo results (see Section 3.3). At 10°S, compared to the observations in the upper 200 m, the model ensemble is substantially cooler in the western half of the basin while it is markedly warmer in the eastern half of the basin (Figures 4b, 4d and 4f), consistent with the common warm bias of coupled models in the southeastern tropical Atlantic (e.g., Richter, 2015; Richter & Tokinaga, 2020). The distinct cold and warm biases are of great magnitude (up to −3.4 and 5.6°C, respectively) and large zonal extent, leading to a low (high) density bias in the eastern (western) side of the basin (Figure 4h), subsequently weakening the simulated basin-wide zonal density gradient in the interior part of the 10°S section considerably. Therefore,
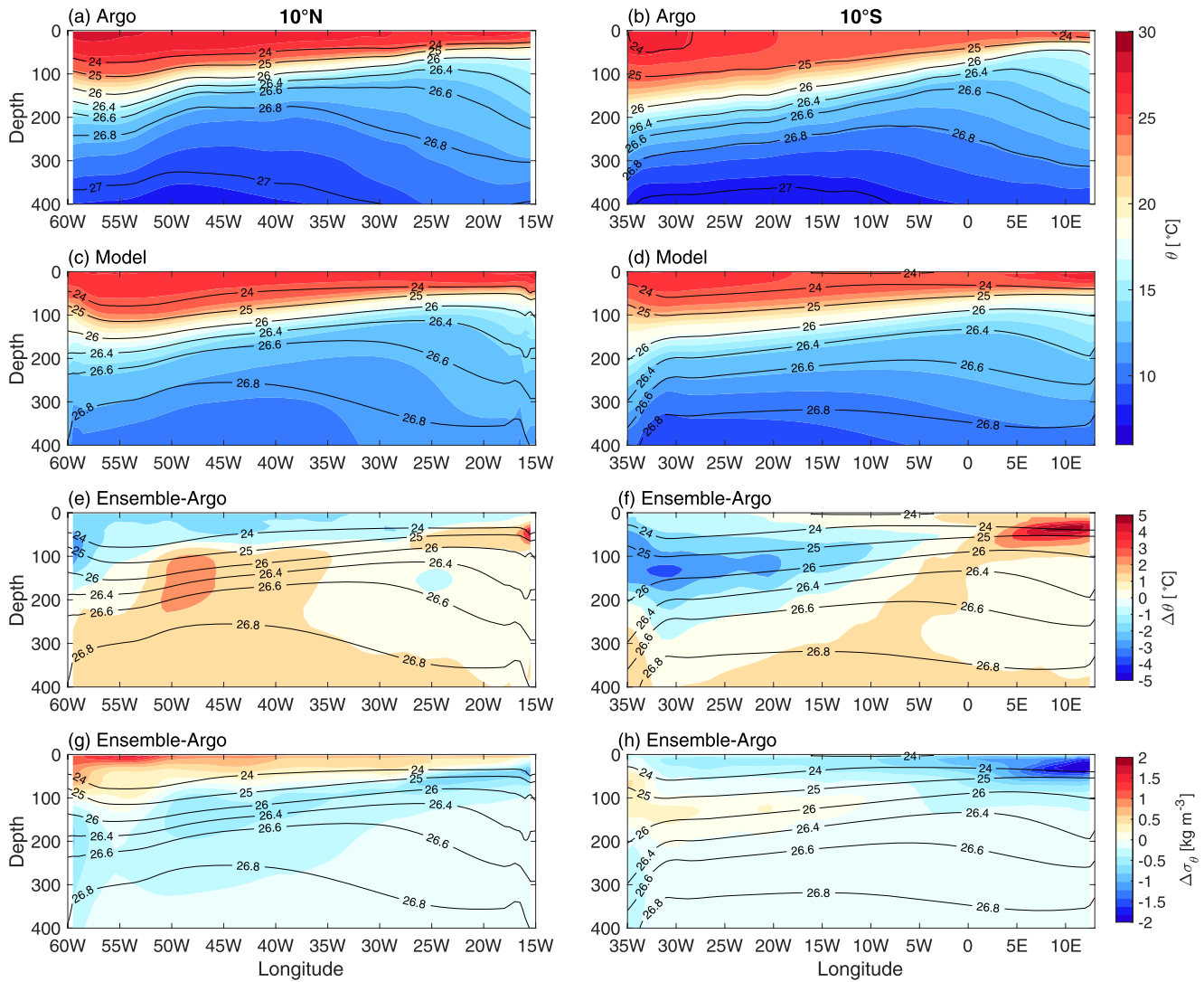
Figure 4. (a and b) Potential temperature (θ in °C, shading) from the Argo climatology and (c and d) model ensemble, and (e and f) the potential temperature difference ($\Delta\theta$ in °C), and (g and h) potential density difference ($\Delta\sigma_\theta$ in kg m^{-3}) between the ensemble and Argo climatology at 10°N (left) and 10°S (right). In (a and b) isopycnals (σ_θ in kg m^{-3}, contours) are estimated from the Argo climatology and in (c–f) from model ensemble.

a weaker ensemble mixed layer and thermocline interior geostrophic transport is anticipated (see Section 3.3 for details).

For salinity, the CMIP6 ensemble at 10°N is generally comparable with the Argo climatology, except for the subtropical underwater (STUW) with maximum salinity occupying the thermocline (Figures 5a and 5c). The STUW in the model ensemble is slightly fresher than in the Argo climatology. The maximum fresh bias is about −0.7 and is mainly located near the western boundary (west of 50°W) between 40 and 120 m (Figure 5e). Below the thermocline, the model ensemble is generally more saline than the Argo climatology. At 10°S, the model ensemble substantially underestimates the observed salinity in the mixed layer and thermocline throughout the entire section (Figures 5b, 5d and 5f). In particular, the maximum fresh bias near the western and eastern boundaries can reach −0.9 and −1.3, respectively. The fresh salinity bias at 10°S may be attributed to excessive precipitation in the Southern Hemisphere (Figure S2 in Supporting Information S1), which is associated with a southward shift of the Intertropical Convergence Zone in the coupled models (Richter et al., 2014; Richter & Tokinaga, 2020). The overall fresh bias in the surface layer reduces the ensemble surface density. In the thermocline, the substantial fresh bias near the western boundary should reduce the density bias caused by the temperature due to density-compensation effect. However, the still existing density bias clearly demonstrates the
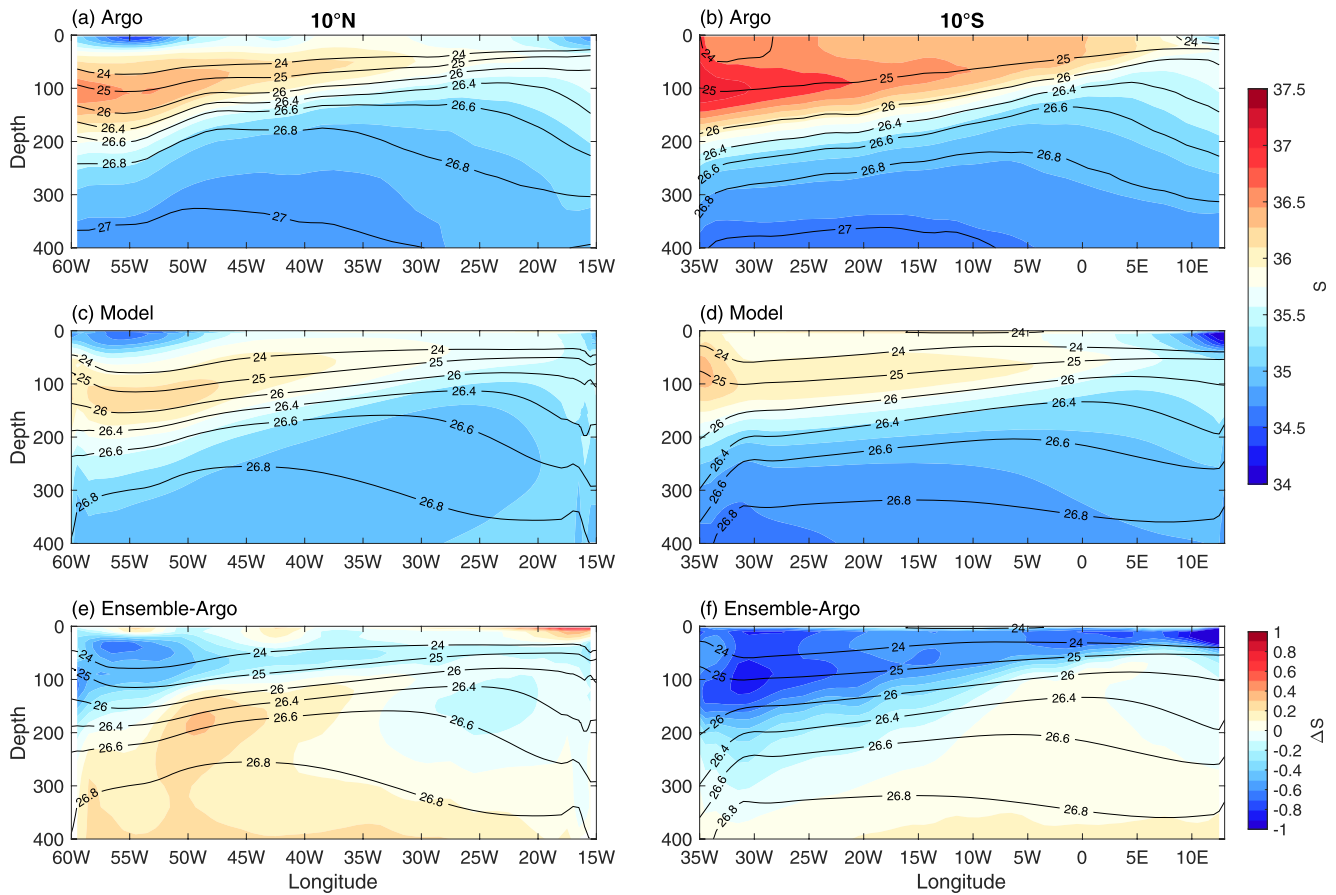
Figure 5. (a and b) Salinity (S, shading) estimated from the Argo climatology and (c and d) model ensemble, and (e and f) their difference (ΔS), at 10°N (left) and 10°S (right). In (a and b) Isopycnals (σ_θ in kg m^{-3}, contours) are estimated from the Argo climatology and in (c–f) from model ensemble.

dominance of temperature in setting the density in the tropical Atlantic (Figure 4h). Note that the aforementioned temperature and salinity biases in the model ensemble are ubiquitous throughout the individual models. For instance, 14 out of the 28 models have a warm potential temperature bias larger than 4°C at about 50°W, 10°N, and, to different degree, all analyzed models simulate a weak temperature-induced zonal density gradient at 10°S.

3.3. Meridional Velocity and Transports at 10°N and 10°S

The meridional geostrophic velocity derived from Argo (updated from Tuchen et al., 2019 by using the high-resolution data) is presented here to compare with the model ensemble meridional total and geostrophic velocity (Figure 6). To further quantify the transports of the different components of the STCs, we also calculate the cumulative transports in the mixed layer and thermocline from the east to the west based on both the model and Argo data (Figure 7). Note that the ensemble geostrophic velocity is generally weaker than the ensemble total velocity at the western boundary. This is due to the fact that the geostrophic velocity at any position is calculated at the center between two adjacent model grids, inevitably resulting in losing velocity information at the boundary region. In the interior below the mixed layer, the ensemble geostrophic velocity (Figure 6) and transport (not shown) agree very well with the ensemble total results, indicating that the interior flow is in geostrophic balance and marginally affected by the subsampling due to geostrophic calculation. Therefore, the geostrophic velocity and transport shown below is only for comparison with the Argo-derived geostrophic results in the mixed layer, and in the thermocline the ensemble total velocity and transport are used.

Overall, the Argo-derived geostrophic velocity shows more variation in the zonal direction compared to the model ensemble. At 10°N, both the Argo and ensemble geostrophic velocity show a distinct northward core (with maximum velocity exceeding 0.20 m s^{-1}) in the upper 100 m west of 57°W characterizing the northward WBC
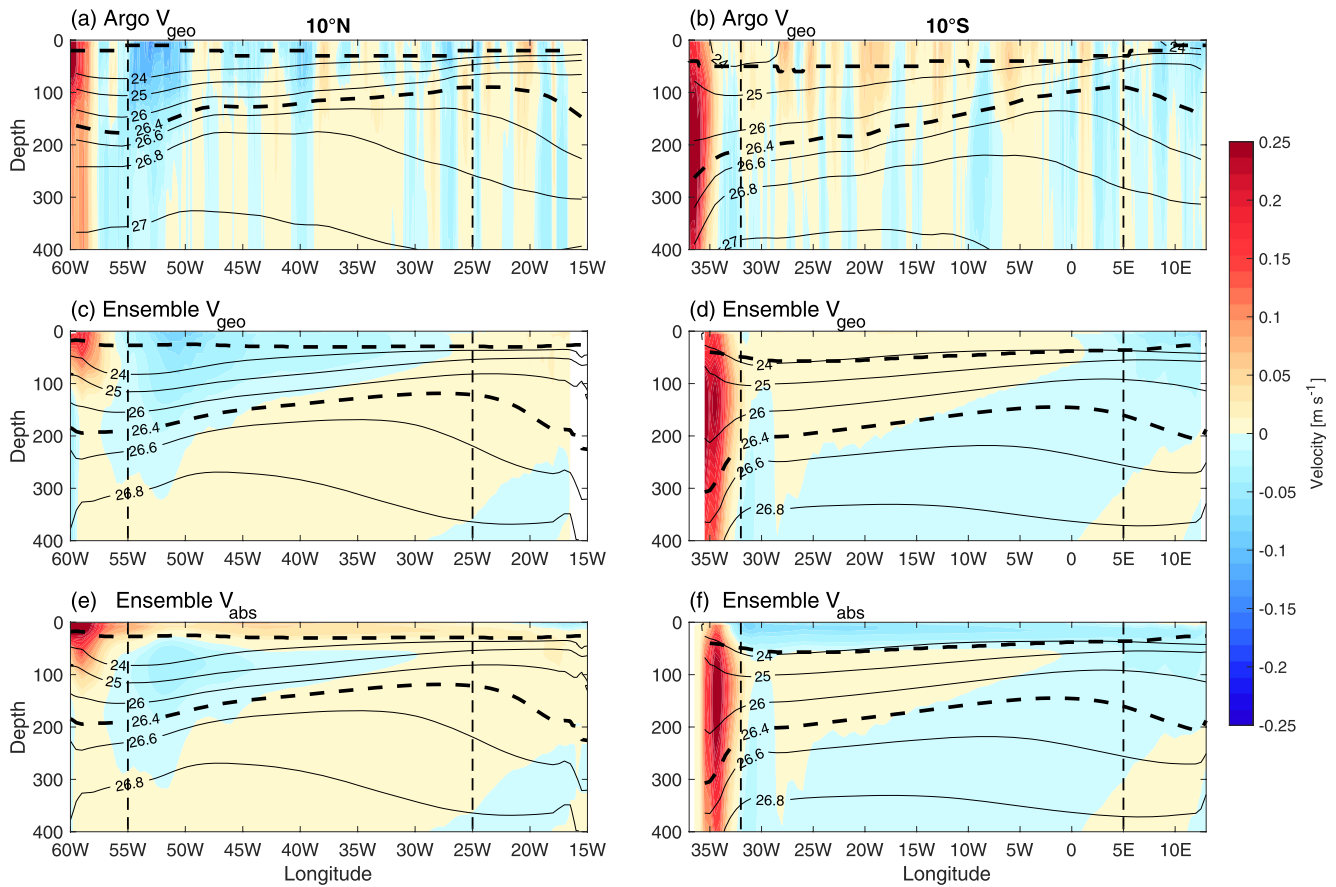
Figure 6. Zonal section of (a and b) mean meridional geostrophic velocity calculated from Argo climatology, (c and d) model ensemble meridional geostrophic velocity, and (e and f) model ensemble total meridional velocity at 10°N (left) and 10°S (right). The thin contour lines are isopycnals (σ_θ in kg m^{-3}) estimated from the respective data. The shallower dashed lines mark the mixed layer depth and the deeper dashed lines mark the 26.4 kg m^{-3} isopycnal. The vertical dashed lines at 55°W and 25°W in (a, d and e) mark the boundaries of the western and eastern boundary region at 10°N, respectively. The vertical dashed lines at 32°W and 5°E mark the boundaries of the western and eastern boundary region at 10°S, respectively.

(Figures 6a and 6c). The ensemble velocity below 100 m is less confined to the boundary and weaker compared to the Argo-derived geostrophic velocity (Figures 6c and 6e). Over the interior and eastern boundary part of the 10°N section, the basin-scale velocity pattern of the model ensemble and Argo geostrophic velocity is comparable. For instance, the geostrophic velocity is primarily southward (northward) above (below) 26.4 kg m^{-3} in both products. Note that the model ensemble velocity does not show the small-scale horizontal variability in the Argo velocity section. This may result from both the relatively low model zonal resolution (about 1°) and ensemble averaging that smooths the velocity field. Between 55°W and 50°W the southward recirculation in the model ensemble appears weaker than in the Argo climatology, which is associated with the warm bias at a similar location (Figure 4e). Therefore, the ensemble thermocline WBC (2.1 ± 1.4 Sv) and interior (−2.7 ± 0.8 Sv, "−" marks southward) transports are markedly weaker than the Argo-derived thermocline WBC (3.8 Sv) and interior (−6.2 Sv) transports (Figure 7c). Fu et al. (2017) showed an intensified western boundary geostrophic velocity band reaching 0.3 m s^{-1} and extending down to 300 m at about 11°N, based on shipboard ADCP and hydrographic observations during a transatlantic section in May 2013. Analysis using the GECCO2 state estimate also indicates a consistent WBC velocity of 0.3 m s^{-1} at 54°W, between 6.5°N and 10°N (Fu et al., 2019).The Argo-derived geostrophic velocity is more consistent with the results by Fu et al. (2017, 2019), while the ensemble WBC appears weaker and mostly concentrated in the upper 100 m.

At 10°S, the NBUC is clearly present in the Argo-derived and ensemble velocity sections (Figures 6b–6f). The NBUC is concentrated in the area west of 32°W and occupies the upper 500 m. Compared to the Argo-derived velocity, the CMIP6 ensemble shows a slightly weaker WBC that occupies a broader zonal range (Figure 6d). Consequently, the ensemble thermocline WBC transport (10.7 ± 3.1 Sv) is consistent with the Argo-derived
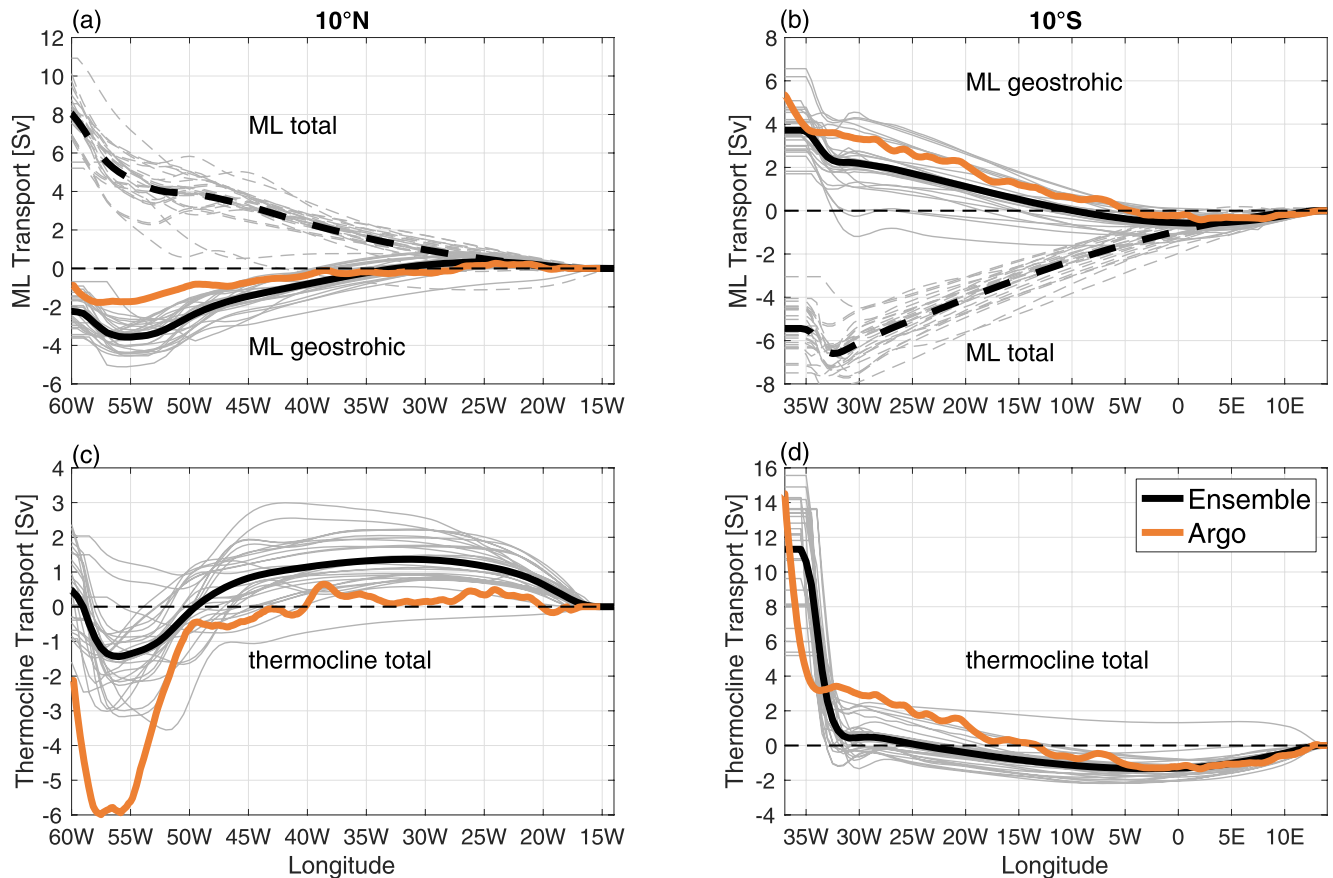
Figure 7. (a and b) Cumulative meridional transport in the mixed layer and (c and d) in the thermocline at 10°N (left) and 10°S (right). In (a and b), the solid thick lines are geostrophic transports calculated from Argo (orange) and model ensemble (black), the dashed thick lines are ensemble total transports. In (c and d), the orange thick lines are Argo geostrophic transports, and the black thick lines are ensemble total transports. All transports are integrated from the eastern to the western boundary. The thin gray lines are estimates of the individual models.

WBC transport (11.3 Sv, Figure 7d). However, in the interior due to the weaker zonal density gradient at 10°S (Figure 4d), the ensemble northward flow in the mixed layer and thermocline is markedly weaker compared to the observations (Figures 6b and 6d). This is particularly evident in the cumulative geostrophic transports in the mixed layer and thermocline layer between 32°W and 5°W at 10°S (Figures 7b and 7d). As a result, the total ensemble thermocline transport is 11.3 ± 2.9 Sv, which is about 3.2 Sv lower than the total Argo thermocline transport.

In summary, the ensemble mixed layer geostrophic transports at both latitudes are equatorward, resulting in a convergence of 5.2 ± 2.1 Sv, which opposes the ensemble Ekman divergence of 18.9 ± 2.5 Sv. This results in a total mixed layer divergence of 13.7 ± 1.7 Sv. The ensemble total mixed layer divergence is in good agreement with the observed total mixed layer divergence of 14.6 ± 3.4 Sv by Tuchen et al. (2019). It is also consistent with the theoretical consideration by Schott et al. (2004) that the trade-winds-induced Ekman divergence is compensated by a geostrophic convergence in the upper layer. The geostrophic compensation is expected to be less strong and unable to reverse the Ekman divergence. The ensemble thermocline convergence is 10.8 ± 2.8 Sv with the southern STC branch accounting for 11.3 ± 2.9 Sv northward transport, and the northern STC branch for 0.6 ± 1.1 Sv northward transport.

3.4. Equatorial Undercurrent at 23°W

The equatorial Atlantic Ocean is characterized by energetic zonal currents. One of the most prominent features is the eastward EUC. The EUC is largely fed by the convergence of the thermocline equatorward flow through western boundary currents and interior geostrophic transports (Schott et al., 2004) and supplies water to the eastern
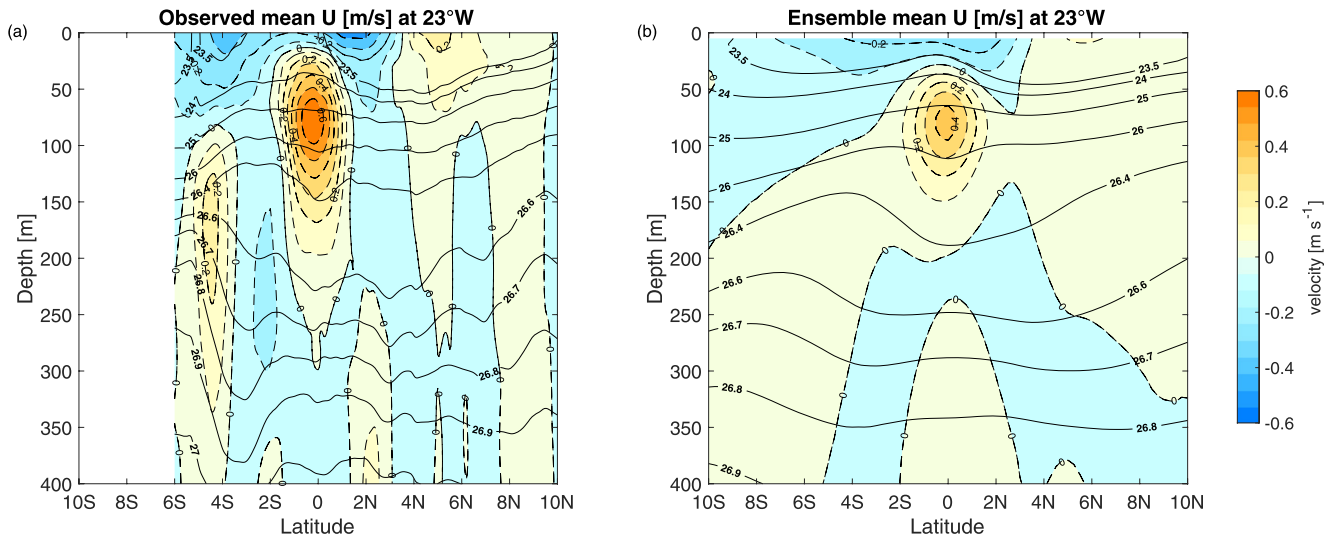
Figure 8. Meridional section of zonal velocity at 23°W estimated from (a) mean shipboard ADCP observations and (b) the model ensemble. Contour lines mark isopycnals (σ_θ in kg m^{-3}) estimated using hydrographic data from shipboard measurements in (a) and the density field of the model ensemble in (b).

equatorial upwelling region. Therefore, the EUC is regarded as a key component of closing the STC loop. Here, we first show the mean zonal velocity section derived from shipboard ADCP observations of 31 cruises along 23°W (Figure 8a). The observed mean EUC has a maximum speed of 0.68 m s^{-1} with its core centered at about 80 m. The EUC core is asymmetric about the equator with slightly higher velocity to the south of the equator. On both sides of the equator from 6°S to about 3°N, branches of the westward South Equatorial Current (SEC) are clearly evident in the upper 200–300 m, with the central SEC south and the northern SEC north of the EUC. In addition, below the EUC, the westward Equatorial Intermediate Current (EIC) is located. On both sides of the EIC, the eastward Southern and Northern Intermediate Countercurrents (SICC and NICC) with a depth larger than 350 and 250 m, respectively, occupy the intermediate layer.

In agreement with the observations, the model ensemble at 23°W also shows an EUC core centered at about 80 m around the equator (Figure 8b). However, the ensemble EUC maximum velocity is only about 0.42 m s^{-1}, substantially weaker than the observation. As the spatial extent of the ensemble EUC is only slightly broader in comparison to the observations, the ensemble EUC transport (12.7 ± 3.5 Sv) is smaller than the observed mean EUC strength (14.8 Sv). The westward SEC branches are also weaker and less deep-reaching in the model ensemble. The intermediate current system (i.e., EIC, SICC, and NICC) is not well resolved and indistinguishable from each other in the model ensemble, likely due to the coarse model resolution. Note that not all the models simulate a weak EUC. We find 14 out of 28 models used in this study with maximum zonal velocity at 23°W between 2°N and 2°S higher than 0.5 m s^{-1}, while the other 14 models have maximum zonal velocity smaller than 0.5 m s^{-1}. This indicates a large inter-model spread in the simulated EUC strength. In the next section, we will investigate the inter-model links between the different STC components and the EUC.

4. Inter-Model Spread of the Simulated Atlantic STC Components

As shown in the previous section, there is a pronounced inter-model spread in the simulated Ekman transport, mixed layer and thermocline transport as well as EUC strength. Since these components are connected to complete the STC loop, we investigate the inter-model links between these STC components as well as between the STCs and the AMOC.

4.1. Relationship Between the Ekman Divergence, Geostrophic Convergence and EUC

The mean Ekman divergence between 10°N and 10°S is first compared with the mean mixed layer and thermocline geostrophic convergence and the EUC transport among the models (Figure 9). First, the comparison shows that models with stronger mean Ekman divergence tend to exhibit a stronger mixed layer geostrophic convergence
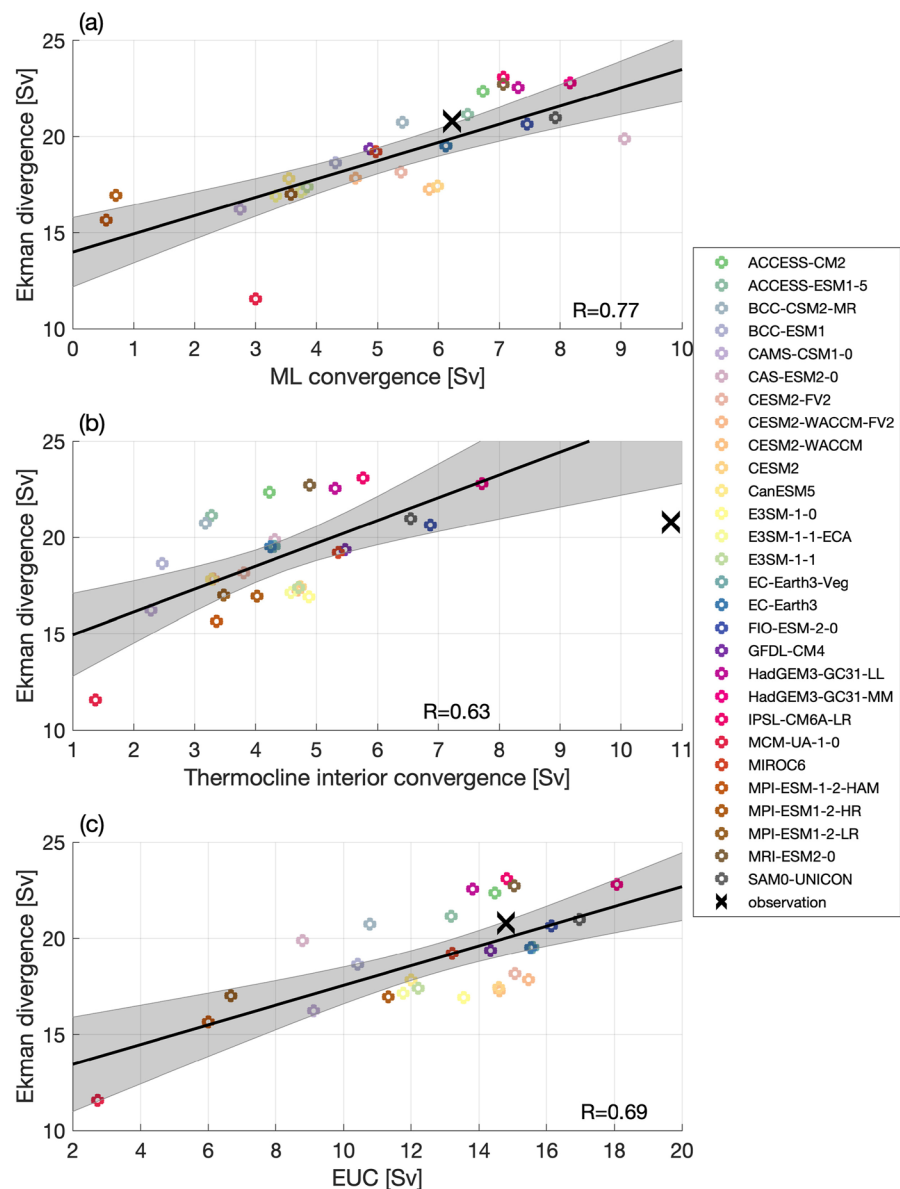
Figure 9. Relationship of Ekman divergence and (a) mixed layer geostrophic convergence, (b) thermocline interior convergence and (c) Equatorial Undercurrent transport. The inter-model correlation R is shown in the lower right corner of each subplot. The correlations are significant at the 95% confidence interval. The black line is calculated from the linear regression between the corresponding components in each subplot. The 95% uncertainty is given as gray shading. The black × marks the observational values of the corresponding variables.

and that the mean mixed layer geostrophic convergence values are less than half of the mean Ekman divergence values (Figure 9a). The inter-model correlation coefficient between these two terms is $R = 0.77$ (significant at the 95% confidence interval). This, again, illustrates that the geostrophic flow in the upper layer counteracts the surface Ekman divergence but is not strong enough to fully compensate it (see e.g., Schott et al., 2004).

Second, the mean Ekman divergence is positively correlated ($R = 0.63$) with the mean interior thermocline geostrophic convergence (Figure 9b), but is not significantly correlated with the total or WBC thermocline convergence (not shown, $R = -0.17$ and -0.35, respectively). Although WBC transports must be considered with respect to total mass balance of the STCs, this result indicates that the WBC transports are not directly related to the surface Ekman divergence in terms of long-term model mean. Further examination indicates that the very strong WBC transport at 10°S (Figure 7d) dominates the total and WBC thermocline convergence. The Sverdrup
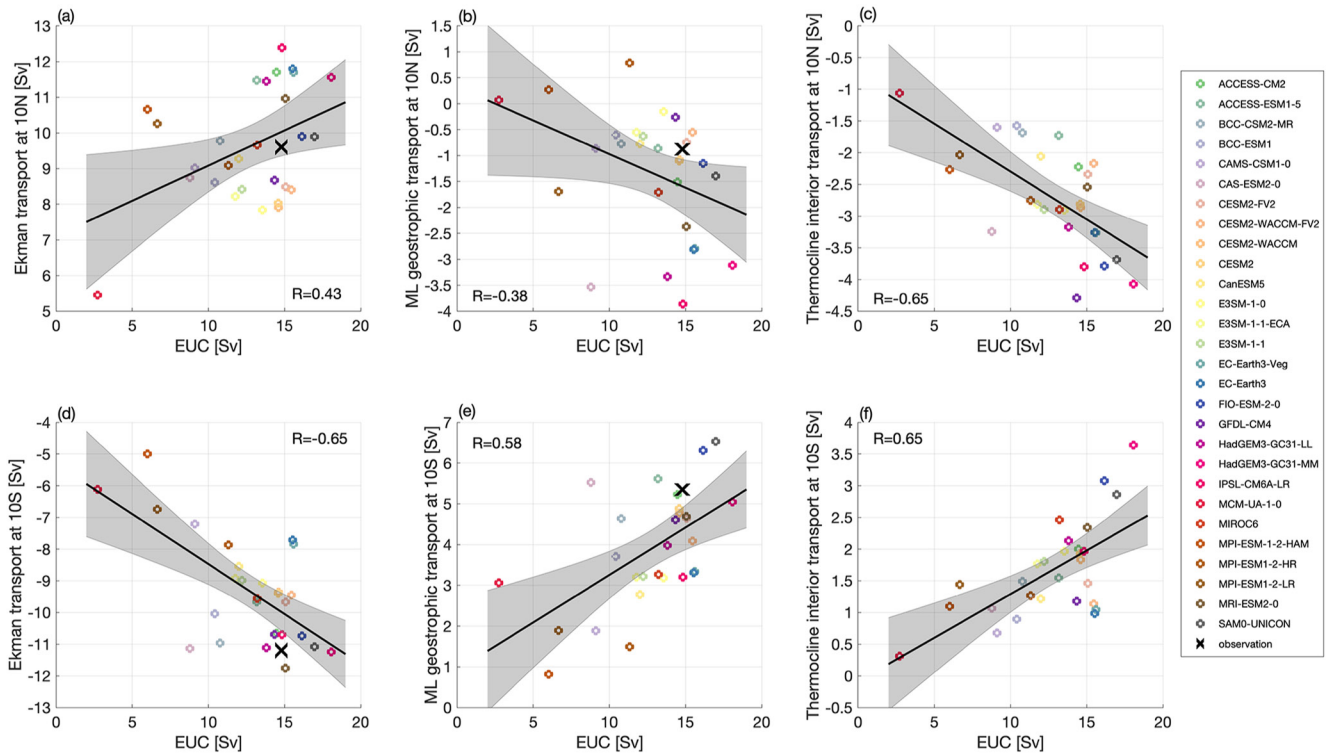
Figure 10. Relationship of Equatorial Undercurrent transport at 23°W and Ekman transport at (a) 10°N and (d) 10°S, mixed layer geostrophic transport at (b) 10°N and (e) 10°S, and thermocline layer interior transport at (c) 10°N and (f) 10°S. The inter-model correlation R is shown in each subplot. The correlations in (c–f) are significant at the 95% confidence interval. The black line is calculated from the linear regression between the corresponding components in each subplot. The 95% uncertainty is given as gray shading. The black × marks the observational values of the corresponding variables. For (c and f), the observed thermocline interior transports from Argo (−6.2 Sv at 10°N and 4.6 at 10°S) are substantially larger than any of the individual model estimates and not marked in the plots.

transport calculated from the model wind stress also shows no significant inter-model correlation with thermocline WBC transports at 10°N and 10°S (not shown, $R = 0.15$ and 0.27, respectively). This may be due to the fact that the WBC in the models is more directly linked to the AMOC rather than to the STCs (see Section 4.3).

Additionally, the mean EUC strength is positively correlated ($R = 0.69$) with the mean Ekman divergence among the models (Figure 9c). This indicates that models with stronger long-term mean Ekman divergence tend to have a stronger mean EUC. Given the positive relationships between the mean Ekman divergence and geostrophic convergences mentioned above, it is not surprising that models with stronger mixed layer geostrophic convergence and thermocline interior convergence also tend to have a stronger EUC (not shown, $R = 0.60$ and $R = 0.73$, respectively).

4.2. Relationship Between the EUC and Hemispheric STC Components

Considering the broad inter-model spread of the mean EUC strength, we further investigate which STC loop components in the Northern and Southern Hemispheres are related to weak and strong mean EUC transports (Figure 10). For the Northern Hemisphere, the mean EUC strength at 23°W is not significantly correlated with the mean Ekman transport ($R = 0.43$, Figure 10a) and mixed layer geostrophic transport ($R = −0.38$, Figure 10b), while it is negatively correlated with the thermocline interior transport ($R = −0.65$, Figure 10c) among the models. Note that the thermocline interior transports at 10°N are southward. The negative correlation suggests that enhanced mean thermocline interior geostrophic transports are associated with a strengthened mean EUC among the models.

For the Southern Hemisphere on the other hand, the mean EUC strength at 23°W is significantly correlated with the mean Ekman transport ($R = −0.65$, Figure 10d), mixed layer geostrophic transport ($R = 0.58$, Figure 10e) and thermocline interior transport ($R = 0.65$, Figure 10f) at 10°S. Note that the Ekman transports at 10°S are
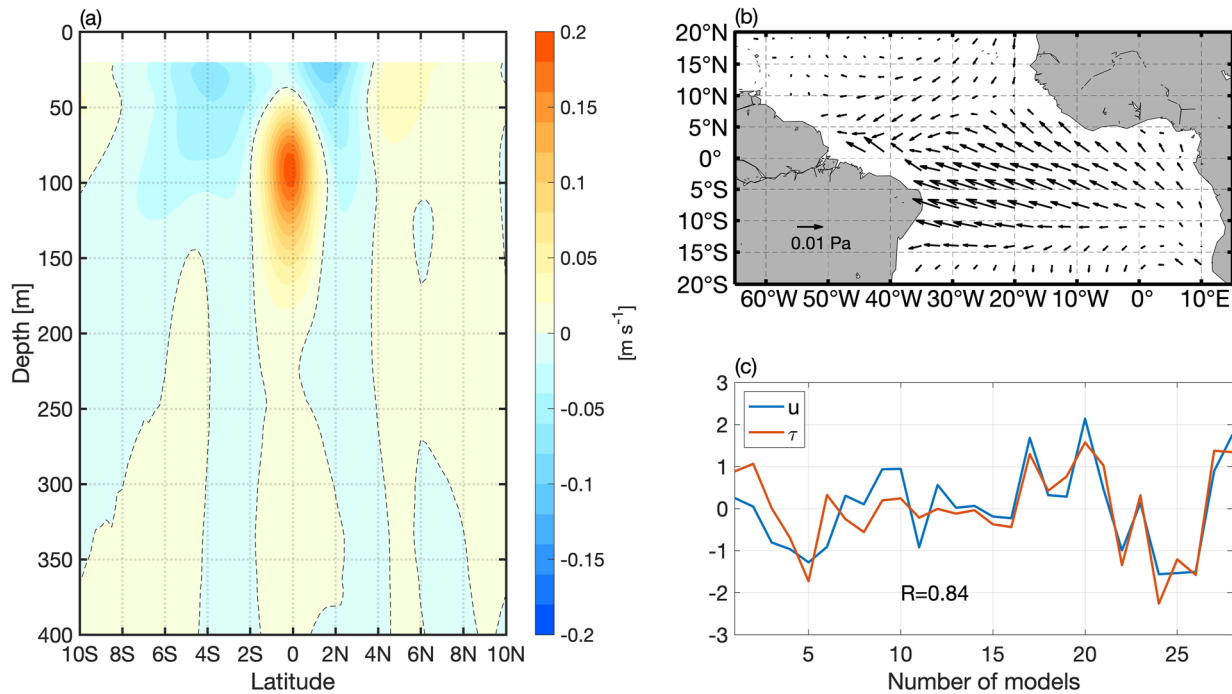
Figure 11. (a) The first mode of inter-model singular value decomposition analysis between zonal velocity at 23°W and (b) wind stress over the tropical Atlantic. The corresponding principal components for zonal velocity (blue) and wind stress (red) are shown in (c). The explained variance of the first singular value decomposition mode is 0.48.

southward, while the mixed layer geostrophic and thermocline interior transports are northward. The correlations suggest that the southern STC components are closely related to the models' EUC strength.

An inter-model singular value decomposition (SVD) analysis between the zonal velocity at 23°W and wind stress in the tropical Atlantic (Figure 11) further illustrates that the intensity of the Southern Hemisphere trade winds largely explains the inter-model spread of the EUC strength. The first inter-model SVD mode (with 0.48 explained variance) of the zonal velocity at 23°W clearly resembles the simulated zonal velocity pattern, that is, an intensified eastward velocity core at the location of the EUC and upper-layer westward current bands laying on both sides of the equator (i.e., the cSEC and the nSEC). Correspondingly, the first mode of wind stress shows the markedly large northwestward wind pattern over the equator and the tropical South Atlantic, where the Southern Hemisphere trade winds prevail. This result suggests that the intensity of the EUC and equatorial zonal currents are strongly coupled with the strength of the Southern Hemisphere trade winds among these models. The Southern Hemisphere trade winds in the model ensemble is located to the south of the observed position (Figure S1 in Supporting Information S1), resulting in a systematically weaker simulated Ekman transport at 10°S than the observed one (Figure 3b). Provided that trade-wind-induced poleward Ekman transports are the driver of the Atlantic STCs, we conclude that the simulated weaker EUCs (Figure 8) as well as smaller South Atlantic mixed layer and thermocline geostrophic transports (Figures 7b and 7d) among the models may be attributed to the weak southeast trade winds.

4.3. Relationship Between the STCs and the AMOC

In order to investigate whether the inter-model spread of the STC strength and the STC components are associated with a corresponding spread of the AMOC, we define the AMOC strength as the maximum of the overturning streamfunction (Figure 2) between 200 and 2,000 m. We use the Ekman divergence between 10°S and 10°N to represent the total STC strength. Here we compare the AMOC strength at 10°S with the total STC strength, the STC components at 10°S, and the EUC at 23°W of the models.

We find no clear pattern in the scatter plot between the STC strength and the AMOC strength (not shown, $R = -0.19$) nor between the EUC and the AMOC ($R = -0.14$) among the models. In contrast, the mean total
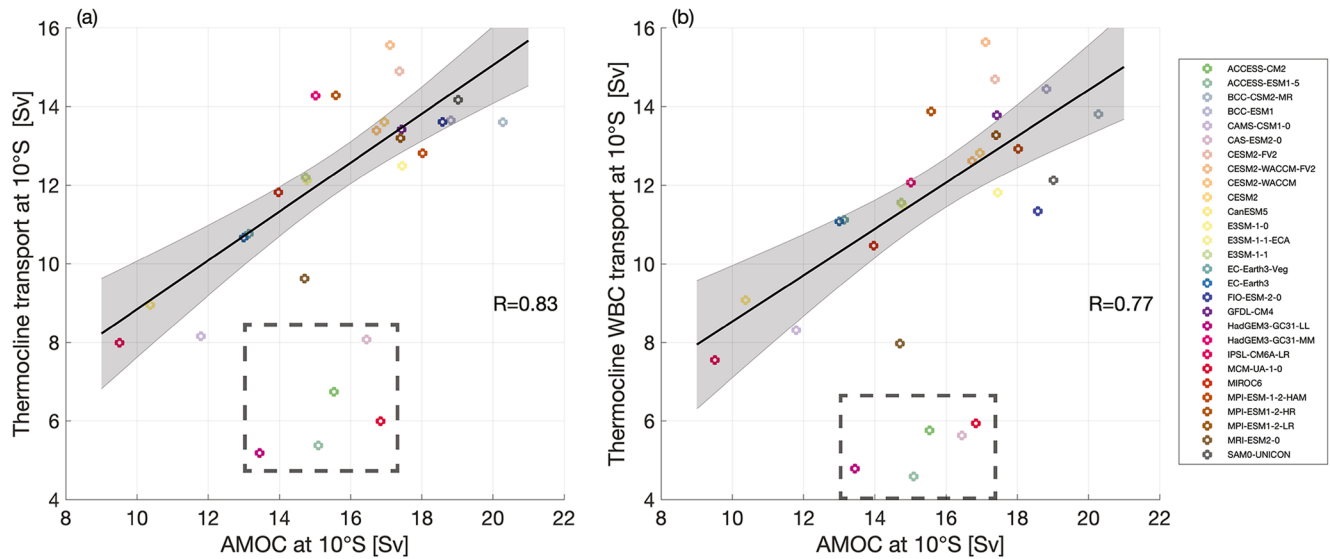
Figure 12. Inter-model relationship (a) between the Atlantic Meridional Overturning Circulation (AMOC) and total thermocline transport at 10°S and (b) between the AMOC and thermocline western boundary current (WBC) transport at 10°S. The correlations are significant at the 95% confidence interval. The black line is calculated from the linear regression between the corresponding components in each subplot. The 95% uncertainty is given as gray shading. Note that the correlations and linear regressions presented in the figures are calculated excluding MCM-UA-1-0, CAS-ESM2-0, ACCESS-CM2, ACCESS-ESM1-5, and HadGEM3-GC31-LL (marked by the black dashed box) due to their exceptionally weak thermocline WBC transport.

thermocline transports at 10°S are highly correlated ($R = 0.83$) with the mean AMOC strengths at 10°S among the models (Figure 12a). This close relationship can be largely attributed to the NBUC transport at 10°S that is the major component of the AMOC upper limb at this latitude and thus well correlated ($R = 0.77$) with the mean AMOC strength among the models (Figure 12b). Note that the inter-model correlations here are calculated using 23 out of the 28 models used in this study. The five exceptions are MCM-UA-1-0, CAS-ESM2-0, ACCESS-CM2, ACCESS-ESM1-5, and HadGEM3-GC31-LL, whose thermocline WBC transports are much weaker compared to the other models. Including these five models strongly reduces the inter-model correlation between the thermocline transport and the AMOC at 10°S to 0.55 (still significant on the 95% confidence interval). As previously noted, it is the interior part of the thermocline transports that is connected to the spread of the mean Ekman divergences and EUC strengths among the models rather than the WBC transports. These results together indicate the distinct contributions of the WBC and interior thermocline transports to the AMOC and the STC in the South Atlantic among the models, respectively.

5. Discussion

In this study, we investigated the mean state of the Atlantic STCs and the inter-model spread and relationships between the STC components in the CMIP6 models. We selected 10°N and 10°S as the latitudes to examine the simulated meridional Ekman transports, the hydrographic structures, and the mixed layer and thermocline transports of the northern and southern STC branches. We also examined the simulated EUC at 23°W, as the EUC completes the STC loop by transporting the thermocline water converging mostly in the western equatorial Atlantic eastward, thereby supplying the equatorial upwelling in the eastern equatorial Atlantic.

At 10°N, the ensemble Ekman transport agrees very well with the mean Ekman transport estimated using NCEP/CFSR and ASCAT wind stress (Figure 3a). The ensemble mean sections of potential temperature and salinity are generally in good agreement with the Argo observations except for west of about 50°W, where the model ensemble is substantially warmer than indicated by observations (Figures 4a and 4c). This leads locally to a too weak zonal density gradient and thus to a too weak equatorward thermocline transport between 55°W and 50°W (Figures 7a and 7c). The CMIP6 ensemble WBC transports in the thermocline (2.1 ± 1.4 Sv) west of 55°W is also weaker than the Argo-derived results (3.8 Sv), but closer to an estimate of about 1.0 Sv (Tuchen et al., 2019) based on the Monthly Isopycnal and Mixed-layer Ocean Climatology (MIMOC, Schmidtko et al., 2013). Note that MIMOC contains hydrographic data observed by CTD profiles close to the boundary and utilizes a boundary

current mapping algorithm. Due to the fact that there is no long-term direct observation at the WBC, it is difficult to conclude which estimate best represents the WBC at 10°N.

At 10°S, there are clear biases in the ensemble hydrographic properties and transport components compared to the observations. In particular, the ensemble Ekman transport is substantially weaker than the observed Ekman transport throughout the basin (Figure 3b). This is accompanied by a basin-wide weaker west-to-east density gradient in the mixed layer and thermocline of the model ensemble than in Argo. The weak ensemble density gradient is primarily caused by a warm bias of temperature in the eastern tropical Atlantic basin and a cold bias in the western basin (Figures 4b and 4d). The temperature bias is consistent with the tropical Atlantic SST biases in the CMIP6 models reported by Richter and Tokinaga (2020). The weak zonal density gradient at 10°S results in a markedly weaker ensemble equatorward geostrophic transport in the interior part of the mixed layer and thermocline than that derived from Argo. The ensemble thermocline WBC transport (10.7 ± 3.2 Sv) at 10°S, on the other hand, is comparable to the Argo-derived thermocline WBC transport (11.3 Sv, Figure 7d), indicating that the model ensemble may represent a reasonable WBC transport in the thermocline at 10°S.

The CMIP6 ensemble EUC at 23°W (maximum core velocity of 0.42 m s^{-1} and transport of 12.7 ± 3.5) is weaker than the observed mean EUC at the same longitude (maximum core velocity of 0.68 m s^{-1} and transport of 14.8 Sv). Examination of the inter-model relationship between different STC loop components links the simulated EUC bias at 23°W mainly to biases of the southern STC branch (Figure 10). This is consistent with previous studies showing that the EUC is primarily supplied by thermocline water from the Southern Hemisphere (Fratantoni et al., 2000; Hazeleger & Drijfhout, 2006). An inter-model SVD analysis between the zonal velocity at 23°W and wind stress in the tropical Atlantic indicates that an enhanced EUC is associated with strengthened southeasterly trade winds in the equatorial and tropical South Atlantic (Figure 11). The trade winds are considered as the forcing of the STCs in both hemispheres. These results together suggest that the generally weak winds over the tropical South Atlantic in the coupled models (Figure S1 in Supporting Information S1) may be responsible for the simulated weak southern STC components and EUC. In addition, model horizontal and vertical resolution as well as applied parameterizations of horizontal and vertical diffusion may also play a role in determining the EUC strength. As an example, "HadGEM3-GC31-MM" has the highest horizontal and vertical resolution (0.25° × 0.25°, 75 vertical levels) among all the models used in this study. This model simulates the strongest EUC (18.1 ± 3.0 Sv, mean ± standard deviation). In comparison, "HadGEM3-GC31-LL", a low resolution version (1° × 1°, 75 vertical levels) of the same model group, simulates a weaker EUC of 13.8 ± 7.3 Sv, despite that it has an Ekman transport of comparible strength at 10°S (−11.1 ± 3.4 Sv for HadGEM3-GC31-LL and −11.2 ± 2.7 Sv for HadGEM3-GC31-MM).

The monthly climatology of the Ekman divergence (Figure 13a) between 10°N and 10°S shows large differences between the model ensemble and NCEP/CFSR in boreal winter (December to February, DJF) and spring (March to May, MAM). The difference in the Ekman divergence mainly arises from 10°S during these seasons (Figures 13c and 13e). This is consistent with the study by Richter and Tokinaga (2020) showing that the equatorial westerly wind bias peaks in MAM and exists not only in coupled models, but also in atmosphere-only versions of the same models that are forced by observed SST. This suggests that the westerly wind bias may originate largely from the atmospheric component of the coupled models, which is further enhanced by the simulated SST bias in the coupled models (Richter et al., 2012). A comparison between the Ekman transport calculated from wind stress of the Atmospheric Model Intercomparison Project (AMIP) models and from CMIP models indicates that the CMIP wind stress at 10°S are strongly weakened when compared to their AMIP counterparts (Figure S3 in Supporting Information S1). Here we identify models with particularly poor representation of the boreal winter and spring Ekman transport at 10°S. These models include MPI-ESM-1-2-HAM, MPI-ESM1-2-LR, EC-Earth3, EC-Earth3-Veg, and CAMs-CSM1-0, whose southward Ekman transports at 10°S are particularly weak compared to the other coupled models and NCEP/CFSR (Figure 13e), while MCM-UA-1-0 shows weaker-than-average Ekman transports in both hemispheres throughout the year. In fact, for the models listed above, not only the climatology but also the standard deviation of the Ekman divergence between 10°N and 10°S and the Ekman transport at 10°S deviates strongly from the results of the other models and NCEP/CFSR in boreal winter and spring (Figures 13b, 13d and 13f). Therefore, caution should be taken when studying the mean state and variability of ocean circulation in the equatorial and tropical South Atlantic based on these models. The results above highlight the impact of atmospheric circulation bias on ocean circulation and emphasize the necessity to improve skills of coupled models to simulate the Southern Hemisphere atmospheric forcing in driving the Atlantic STCs.
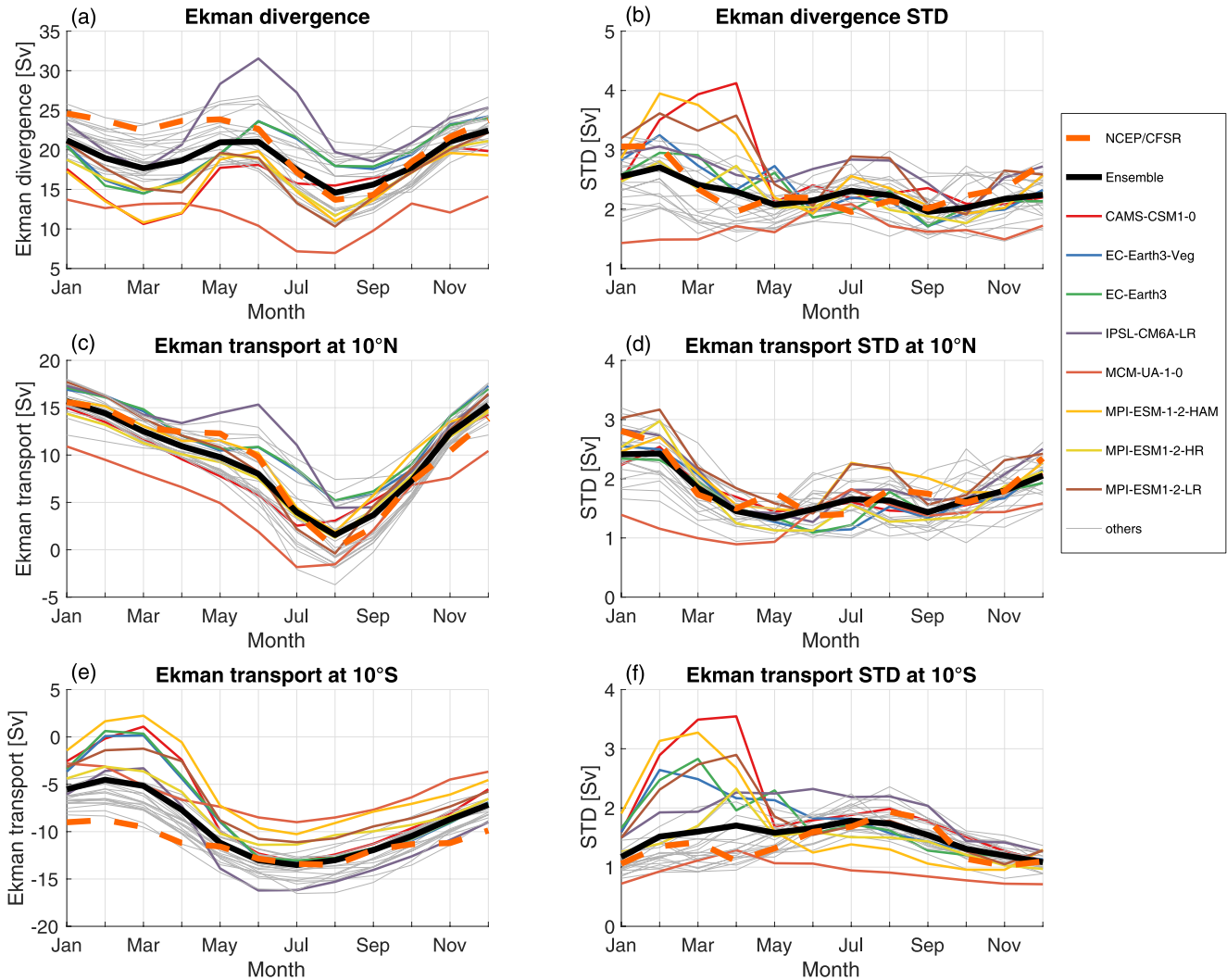
Figure 13. Monthly climatology of (a) Ekman divergence, (b) Ekman divergence standard deviation (STD), (c) Ekman transport at 10°N, (d) Ekman transport STD at 10°N, (e) Ekman transport at 10°S, and (f) Ekman transport STD at 10°S. The thick orange dashed line is the estimates from National Centers for Environmental Prediction Climate Forecast System Reanalysis (NCEP/CFSR), the black thick line is the multi-model ensemble, the colored thin lines mark the models deviating strongly from the NCEP/CFSR. The gray thin lines are the other models used in this study.

Furthermore, we find no direct inter-model relationship between the STC and AMOC strengths in the South Atlantic. In contrast, there is a significant inter-model correlation between the mean thermocline WBC transport and the AMOC strength at 10°S ($R = 0.77$, Figure 12). Note that among the models the time-mean thermocline interior transports at 10°S tend to be correlated with the time-mean Ekman transport at 10°S and the EUC strength. This indicates that the simulated mean-state thermocline WBC and interior flow participate more directly in the AMOC and STC, respectively, and that the mean-state AMOC and STC are decoupled. In addition, we examined the inter-model relationship between the AMOC and the EUC, and find no significant correlation ($R = -0.14$). This is not surprising, since we have shown that the EUC is more related to the southern branch of the STC, while the STC is decoupled from the AMOC.

Note that we used climatological mean of the full historical simulation of each model to calculate the inter-model correlations among the different STC components (Figures 9 and 10) and between the STCs and the AMOC (Figure 12). When the long-term climatology of each individual model is regarded as a realization of the present-day climate, the relationship derived from these 28 realizations not only serves as a tool to identify inter-model spread and biases of the simulated variables, but also, to some extent, reveals the dynamic relationship between these key circulation components in nature. Therefore, further studies are needed to investigate STC
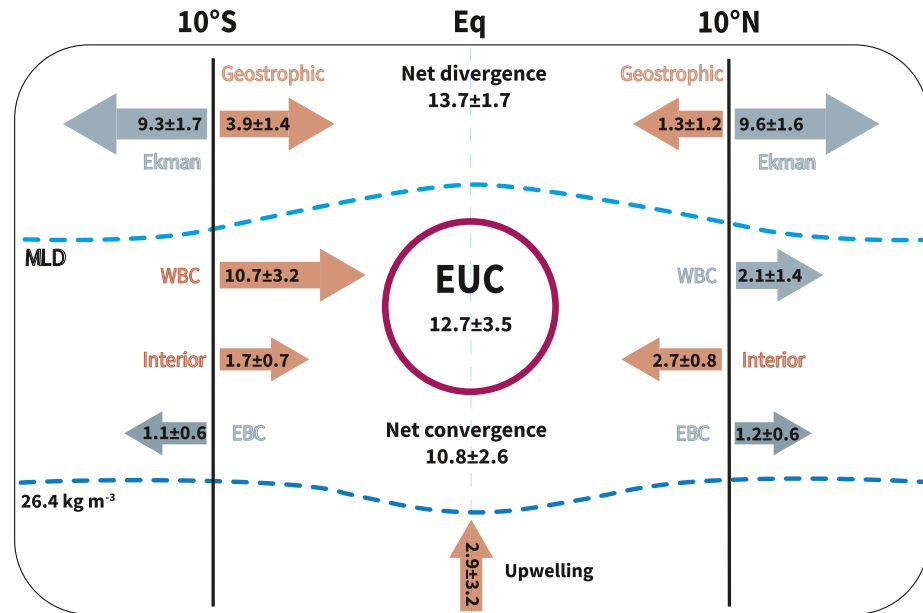
Figure 14. Schematic of mean Subtropical Cell transports (in Sv) among the 28 Coupled Model Intercomparison Project Phase 6 models. mixed layer depth (MLD) is defined by a potential density difference threshold of 0.125 kg m^{-3}. The mean and standard deviation values are determined based on the climatological mean of the 28 models. Within the thermocline (between MLD and 26.4 kg m^{-3}), western boundary current (WBC), interior and eastern boundary current represent transports of the WBC, interior part of the basin, and eastern boundary current, respectively.

temporal variability and the causes and impacts of the variability from a time-varying perspective. It is worth mentioning that the historical model simulations have considerably longer temporal coverage than the observations. When the ensemble and inter-model spread analyses of this study are performed for a time period matching the observational record, that is, 1979–2010 for NCEP/CSFR wind and 2000–2014 for the EUC and Argo measurement, the conclusion of this study still hold true. This further indicates that the model bias and the inter-model links between the STC components are independent of long-term variability and trend.

6. Summary

Finally, the mean state of the STCs as derived from the CMIP6 models is summarized in a schematic (Figure 14). In the mixed layer, the Ekman divergence between 10°N and 10°S accounts for 18.9 ± 2.5 Sv, which is opposed by an geostrophic convergence of 5.2 ± 2.1 Sv. The resulting net mixed layer divergence is 13.7 ± 1.7 Sv. In the thermocline, the geostrophic convergence is 10.8 ± 2.6 Sv, which is dominated by the WBC transport at 10°S (10.9 ± 3.1 Sv). The resultant imbalance between the net mixed layer divergence and thermocline convergence is 2.9 ± 2.8 Sv. This amount of net imbalance in the model must be upwelled from beneath the 26.4 kg m^{-3} isopycnal to the mixed layer as part of the northward upper limb of the AMOC coming from the South Atlantic, consistent with observations (e.g., Tuchen et al., 2019; Zhang et al., 2003). Note that the inter-model correlation between the net imbalance and the AMOC and STC (Ekman divergence) is of similar magnitude but of reversed sign ($R = -0.65$ and $R = 0.58$, respectively), indicating a net imbalance increasing with STC strength and the compensation of the net imbalance increasing with AMOC strength. In addition, the EUC at 23°W carries 12.7 ± 3.5 Sv water eastward to supply the eastern tropical upwelling. Finally, despite the discussed biases in the simulated South Atlantic trade winds, EUC, and partition between the interior and WBC parts of the thermocline layer transports, the model ensemble net mixed layer divergence, that is, 13.7 ± 1.7 Sv, thermocline convergence, that is, 10.8 ± 2.6 Sv, and the required upwelling, that is, 2.9 ± 2.8 Sv, are in very good agreement with the observational estimates (14.9 ± 3.4 Sv, 11.9 ± 1.7, and 2.7 ± 3.8 Sv, respectively) by Tuchen et al. (2019). This indicates that the model ensemble retains the bulk of the observed mean STC circulation. Note that the net freshwater input into the region between 10°N and 10°S due to precipitation, evaporation and river run-off (Dai & Trenberth, 2003) is neglected in this balance.

This study provides the first assessment of the simulated Atlantic STCs in the CMIP6 models with respect to the mean state, inter-model spread and link of the STC loop components. The results give insights into simulated circulation biases and the possible causes related to atmospheric forcing in the tropical Atlantic. This provides a reference for further studies on Atlantic STC variability and STCs' dynamic relationship with other climate-related variables and indices, such as the AMOC and tropical Atlantic SST variability. This study also sets a baseline for evaluating STCs' possible changes in the future using coupled climate models.

Data Availability Statement

The Argo data were collected and made freely available by the International Argo Program and the national programs that contribute to it (http://www.argo.ucsd.edu, http://argo.jcommops.org). The CMIP6 model data are available from the World Climate Research Programme at https://esgf-data.dkrz.de/projects/cmip6-dkrz/. The NCEP/CFSR wind stress data are available at https://rda.ucar.edu/datasets/ds093.0/. The ASCAT wind stress data are available via CMEMS at https://marine.copernicus.eu/. The Argo climatology is available at http://sio-argo.ucsd.edu/RG_Climatology.html. The mean zonal velocity section at 23°W is available at https://doi.org/10.5281/zenodo.4478285.

References

Brandt, P., Bange, H. W., Banyte, D., Dengler, M., Didwischus, S. H., Fischer, T., et al. (2015). On the role of circulation and mixing in the ventilation of oxygen minimum zones with a focus on the eastern tropical North Atlantic. *Biogeosciences*, *12*(2), 489–512. https://doi.org/10.5194/bg-12-489-2015

Brandt, P., Hahn, J., Schmidtko, S., Tuchen, F. P., Kopte, R., Kiko, R., et al. (2021). Atlantic Equatorial Undercurrent intensification counteracts warming-induced deoxygenation. *Nature Geoscience*, *14*(5), 278–282. https://doi.org/10.1038/s41561-021-00716-1

Dai, A., & Trenberth, K. E. (2003). New estimates of continental discharge and oceanic freshwater transport. In *AMS symposium on observing and understanding the variability of water in weather and climate* (Vol. 9–13). Retrieved from http://www.cgd.ucar.edu/cas/adai/papers/Dai_discharge_AMS03.pdf

Decker, M., Brunke, M. A., Wang, Z., Sakaguchi, K., Zeng, X., & Bosilovich, M. G. (2012). Evaluation of the reanalysis products from GSFC, NCEP, and ECMWF using flux tower observations. *Journal of Climate*, *25*(6), 1916–1944. https://doi.org/10.1175/JCLI-D-11-00004.1

Duteil, O., Böning, C. W., & Oschlies, A. (2014). Variability in subtropical-tropical cells drives oxygen levels in the tropical Pacific Ocean. *Geophysical Research Letters*, *41*(24), 8926–8934. https://doi.org/10.1002/2014GL061774

Eyring, V., Bony, S., Meehl, G. A., Senior, C. A., Stevens, B., Stouffer, R. J., & Taylor, K. E. (2016). Overview of the coupled model Intercomparison project phase 6 (CMIP6) experimental design and organization. *Geoscientific Model Development*, *9*(5), 1937–1958. https://doi.org/10.5194/gmd-9-1937-2016

Fratantoni, D. M., Johns, W. E., Townsend, T. L., & Hurlburt, H. E. (2000). Low-latitude circulation and mass transport pathways in a model of the tropical Atlantic Ocean. *Journal of Physical Oceanography*, *30*(8), 1944–1966. https://doi.org/10.1175/1520-0485(2000)030<1944:LLCAMT>2.0.CO;2

Fu, Y., Karstensen, J., & Brandt, P. (2017). On the meridional ageostrophic transport in the tropical Atlantic. *Ocean Science*, *13*(4), 531–549. https://doi.org/10.5194/os-13-531-2017

Fu, Y., Wang, C., Brandt, P., & Greatbatch, R. J. (2019). Interannual variability of Antarctic intermediate water in the tropical North Atlantic. *Journal of Geophysical Research: Oceans*, *124*(6), 4044–4057. https://doi.org/10.1029/2018JC014878

Graffino, G., Farneti, R., & Kucharski, F. (2021). Low-frequency variability of the Pacific Subtropical Cells as reproduced by coupled models and ocean reanalyses. *Climate Dynamics*, *56*(9–10), 3231–3254. https://doi.org/10.1007/s00382-021-05639-6

Hazeleger, W., de Vries, P., & Friocourt, Y. (2003). Sources of the equatorial undercurrent in the Atlantic in a high-resolution ocean model. *Journal of Physical Oceanography*, *33*(4), 677–693. https://doi.org/10.1175/1520-0485(2003)33<677:SOTEUI>2.0.CO;2

Hazeleger, W., & Drijfhout, S. (2006). Subtropical cells and meridional overturning circulation pathways in the tropical Atlantic. *Journal of Geophysical Research*, *111*(C3), C03013. https://doi.org/10.1029/2005JC002942

Hummels, R., Brandt, P., Dengler, M., Fischer, J., Araujo, M., Veleda, D., & Durgadoo, J. V. (2015). Interannual to decadal changes in the western boundary circulation in the Atlantic at 11°S. *Geophysical Research Letters*, *42*(18), 7615–7622. https://doi.org/10.1002/2015GL065254

Johnson, G. C., & Zhang, D. (2003). Structure of the Atlantic Ocean equatorial deep jets. *Journal of Physical Oceanography*, *33*(3), 600–609. https://doi.org/10.1175/1520-0485(2003)033<0600:SOTAOE>2.0.CO;2

Karstensen, J., & Quadfasel, D. (2002). Formation of Southern Hemisphere thermocline waters: Water mass conversion and subduction. *Journal of Physical Oceanography*, *32*(11), 3020–3038. https://doi.org/10.1175/1520-0485(2002)032<3020:FOSHTW>2.0.CO;2

Kleeman, R., McCreary, J. P., & Klinger, B. A. (1999). A mechanism for generating ENSO decadal variability. *Geophysical Research Letters*, *26*(12), 1743–1746. https://doi.org/10.1029/1999GL900352

Liu, Z., Philander, S. G. H., & Pacanowski, R. C. (1994). A GCM study of tropical–subtropical upper-ocean water exchange. *Journal of Physical Oceanography*, *24*(12), 2606–2623. https://doi.org/10.1175/1520-0485(1994)024<2606:AGSOTU>2.0.CO;2

Malanotte-Rizzoli, P., Hedstrom, K., Arango, H., & Haidvogel, D. B. (2000). Water mass pathways between the subtropical and tropical ocean in a climatological simulation of the North Atlantic Ocean. *Dynamics of Atmospheres and Oceans*, *32*(3–4), 331–371. https://doi.org/10.1016/S0377-0265(00)00051-8

McCreary, J. P., & Lu, P. (1994). Interaction between the subtropical and equatorial ocean circulations: The subtropical cell. *Journal of Physical Oceanography*, *24*(2), 466–497. https://doi.org/10.1175/1520-0485(1994)024<0466:IBTSAE>2.0.CO;2

McPhaden, M. J., & Zhang, D. (2002). Slowdown of the meridional overturning circulation in the upper Pacific Ocean. *Nature*, *415*(6872), 603–608. https://doi.org/10.1038/415603a

Oschlies, A., Brandt, P., Stramma, L., & Schmidtko, S. (2018). Drivers and mechanisms of ocean deoxygenation. *Nature Geoscience*, *11*(7), 467–473. https://doi.org/10.1038/s41561-018-0152-2

Rabe, B., Schott, F. a., & Köhl, A. (2008). Mean circulation and variability of the tropical Atlantic during 1952–2001 in the GECCO Assimilation fields. *Journal of Physical Oceanography*, *38*(1), 177–192. https://doi.org/10.1175/2007JPO3541.1

Richter, I. (2015). Climate model biases in the eastern tropical oceans: Causes, impacts and ways forward. *WIREs Climate Change*, *6*(3), 345–358. https://doi.org/10.1002/wcc.338

Richter, I., & Tokinaga, H. (2020). An overview of the performance of CMIP6 models in the tropical Atlantic: Mean state, variability, and remote impacts. *Climate Dynamics*, *55*(9–10), 2579–2601. https://doi.org/10.1007/s00382-020-05409-w

Richter, I., Xie, S. P., Behera, S. K., Doi, T., & Masumoto, Y. (2014). Equatorial Atlantic variability and its relation to mean state biases in CMIP5. *Climate Dynamics*, *42*(1–2), 171–188. https://doi.org/10.1007/s00382-012-1624-5

Richter, I., Xie, S. P., Wittenberg, A. T., & Masumoto, Y. (2012). Tropical Atlantic biases and their relation to surface wind stress and terrestrial precipitation. *Climate Dynamics*, *38*(5–6), 985–1001. https://doi.org/10.1007/s00382-011-1038-9

Roemmich, D., & Gilson, J. (2009). The 2004–2008 mean and annual cycle of temperature, salinity, and steric height in the global ocean from the Argo program. *Progress in Oceanography*, *82*(2), 81–100. https://doi.org/10.1016/j.pocean.2009.03.004

Schmidtko, S., Johnson, G. C., & Lyman, J. M. (2013). MIMOC: A global monthly isopycnal upper-ocean climatology with mixed layers. *Journal of Geophysical Research: Oceans*, *118*(4), 1658–1672. https://doi.org/10.1002/jgrc.20122

Schott, F. A., Dengler, M., Zantopp, R., Stramma, L., Fischer, J., & Brandt, P. (2005). The shallow and deep western boundary circulation of the South Atlantic at 5°–11°S. *Journal of Physical Oceanography*, *35*(11), 2031–2053. https://doi.org/10.1175/JPO2813.1

Schott, F. A., McCreary, J. P., & Johnson, G. C. (2004). Shallow overturning circulations of the tropical- subtropical oceans. *Earth's Climate*, 261–304. https://doi.org/10.1029/147GM15

Tuchen, F. P., Brandt, P., Lübbecke, J. F., & Hummels, R. (2022). Transports and pathways of the tropical AMOC return flow from Argo data and shipboard velocity measurements. *Journal of Geophysical Research: Oceans*. https://doi.org/10.1029/2021JC018115

Tuchen, F. P., Lübbecke, J. F., Brandt, P., & Fu, Y. (2020). Observed transport variability of the Atlantic Subtropical Cells and their connection to tropical sea surface temperature variability. *Journal of Geophysical Research: Oceans*, *125*(12), 1–20. https://doi.org/10.1029/2020JC016592

Tuchen, F. P., Lübbecke, J. F., Schmidtko, S., Hummels, R., & Böning, C. W. (2019). The Atlantic Subtropical Cells inferred from observations. *Journal of Geophysical Research: Oceans*, *124*(11), 7591–7605. https://doi.org/10.1029/2019JC015396

Wang, C., & Zhang, L. (2013). Multidecadal ocean temperature and salinity variability in the tropical North Atlantic: Linking with the AMO, AMOC, and subtropical cell. *Journal of Climate*, *26*(16), 6137–6162. https://doi.org/10.1175/JCLI-D-12-00721.1

Zhang, D., McPhaden, M. J., & Johns, W. E. (2003). Observational evidence for flow between the subtropical and tropical Atlantic: The Atlantic Subtropical Cells. *Journal of Physical Oceanography*, *33*(8), 1783–1797. https://doi.org/10.1175/2408.1